

1 MAX-DOAS observations of formaldehyde and nitrogen dioxide at three 2 sites in Asia and comparison with the global chemistry transport model 3 CHASER

4 Hossain Mohamed Syedul Hoque¹, Kengo Sudo^{1,2}, Hitoshi Irie³, Alessandro Damiani³, Manish Naja⁴, and Al
5 Mashroor Fatmi³

6 ¹Graduate School of Environmental Studies, Nagoya University, Nagoya, 4640064, Japan

7 ²Japan Agency for Marine-Earth Science and Technology (JAMSTEC), Kanagawa, 2370061, Japan

8 ³Center for Environmental Remote Sensing (CEReS), Chiba University, Chiba, 2638522, Japan

9 ⁴Aryabhatta Research Institute for Observational Sciences (ARIES), Manora Peak, Nainital-263001, Uttarakhand,
10 India

11

12 *Correspondence to:* Hossain Mohammed Syedul Hoque (hoque.hossain.mohammed.syedul.u6@f.mail.nagoya-
13 u.ac.jp)

14

15 **Abstract.** Formaldehyde (HCHO) and nitrogen dioxide (NO₂) concentrations and profiles were retrieved
16 from ground-based multi-axis differential optical absorption spectroscopy (MAX-DOAS) observations
17 during January 2017 - December 2018 at three sites in Asia: (1) Phimai (15.18°N, 102.5°E), Thailand;
18 (2) Pantnagar (29°N, 78.90°E) in the Indo Gangetic Plain (IGP), India; and (3) Chiba (35.62°N,
19 140.10°E), Japan. Retrievals were performed using the Japanese MAX-DOAS profile retrieval algorithm
20 ver. 2 (JM2). The observations were used to evaluate the NO₂ and HCHO partial columns and profiles (0
21 - 4 km) simulated using the CHASER global chemistry transport model (CTM). At all three sites, the
22 NO₂ and HCHO concentrations showed consistent seasonal variation throughout the investigated period.
23 Biomass burning affected the HCHO and NO₂ variations at Phimai during the dry season and at Pantnagar
24 during spring (March - May) and post-monsoon (September - November). Results found for the HCHO
25 to NO₂ ratio (R_{FN}), an indicator of high ozone sensitivity, indicate that the transition region (i.e., $1 < R_{FN}$
26 < 2) changes regionally, echoing the recent finding for R_{FN} effectiveness. Moreover, reasonable estimates
27 of transition regions can be derived, accounting for the NO₂ - HCHO chemical feedback.

28 The model was also evaluated against global datasets of NO₂ and HCHO columns retrieved from Ozone
29 Monitoring Instrument (OMI) observations. Despite underestimation, the model well simulated the
30 satellite-observed global spatial distribution of NO₂ and HCHO, with respective spatial correlations (*r*)
31 of 0.73 and 0.74, respectively. CHASER demonstrated good performance, reproducing the MAX-DOAS
32 retrieved HCHO and NO₂ abundances at Phimai, mainly above 500 m from the surface. Model results
33 agree with the measured variations within the one sigma standard deviation of the observations.
34 Simulations at higher resolution improved the modeled NO₂ estimates for Chiba, reducing the mean bias
35 error (MBE) for the 0 - 2 km height by 35%, but resolution-based improvements were limited to the
36 surface layers. Sensitivity studies show that pyrogenic emissions at Phimai contribute to the HCHO and
37 NO₂ concentrations, respectively up to 50 and 35%.

38 1 Introduction

39 Formaldehyde (HCHO), the most abundant carbonyl compound in the atmosphere, is a high-yield product
40 of oxidization of all primary volatile organic compounds (VOCs) emitted from natural and anthropogenic
41 sources by hydroxyl radicals (OH). Oxidation of long-lived VOCs such as methane produces a global
42 HCHO background concentration of 0.2 – 1.0 ppbv in remote marine environments (Weller et al., 2000;
43 Burkert et al., 2001; Singh et al., 2004; Sinreich et al., 2005). Aside from oxidation of VOCs, the
44 significant sources of HCHO are direct emissions from biomass burning, industrial processes, fossil fuel
45 combustion (Lee et al., 1997; Hak et al., 2005; Fu et al., 2008), and vegetation (Seco et al., 2007).
46 However, oxidization of non-methane VOCs emitted from biogenic (e.g., isoprene) or anthropogenic (e.g.,
47 butene) sources govern the spatial variation of HCHO on a global scale (Franco et al., 2015). The sinks
48 of HCHO include photolysis at wavelengths shorter than 400 nm, oxidation by OH, and wet deposition,
49 thereby limiting the lifetime of HCHO to a few hours (Arlander et al., 1995).

50 Nitrogen dioxide (NO₂), an important atmospheric constituent, (1) participates in the catalytic
51 formation of tropospheric ozone (O₃), (2) acts as a catalyst for stratospheric ozone (O₃) destruction
52 (Crutzen, 1970), (3) contributes to the formation of aerosols (Jang and Kamens, 2001), (4) acts as a
53 precursor of acid rain (Seinfeld and Pandis, 1998), and (5) strongly affects radiative forcing (Solomon et
54 al. 1999; Lelieveld et al., 2002;). Nitrogen oxides (NO_x = NO (nitric oxide) + NO₂) are emitted from
55 natural and anthropogenic sources. Primary NO_x emission sources include biomass burning, fossil fuel

56 combustion, soil emissions, and lightning (Bond et al., 2001; Zhang et al., 2003). Not only do NO_x
57 emissions degrade air quality; they are leading air pollutant (Ma et al., 2013). Both HCHO and NO_2 are
58 important intermediates in the global VOC– HO_x (hydrogen oxides)– NO_x catalytic cycle, which governs
59 O_3 chemistry in the troposphere (Lee et al., 1997; Houweling et al., 1998; Hak et al., 2005; Kanakidou et
60 al., 2005). Thus, both trace gases play crucially important roles in tropospheric chemistry.

61 The observational sites examined for the present study have different atmospheric characteristics.
62 Thailand is strongly affected by pollution because of rapid economic development and urbanization.
63 Moreover, biomass burning in Southeast Asia is a significant source of O_3 precursors, contributing up to
64 30% of the total concentrations during the peak burning season (Amnuaylorajen et al., 2020; Khodmanee
65 et al. 2021). Because of rapid industrialization, India the second most populous country in the world, is
66 witnessing an increasing O_3 trend along with NO_2 and HCHO concentrations in all major cities (Mahajan
67 et al; 2015; Lu et al, 2018;). The Indo-Gangetic Plain (IGP), which covers ~21% of the Indian
68 subcontinent land area is hotspots of severe air pollution (Giles et al; 2005, Biswas et al; 2019). In contrast,
69 surface O_3 concentrations have shown an increasing trend in Japan, despite decreasing NO_x and VOC
70 concentrations related to emission control measures after 2000 (Irie et al., 2021). Therefore, observational
71 and modeling studies must be conducted to improve our quantitative understanding of the O_3 – NO_x –VOC
72 relation in these regions.

73 Multi-axis differential optical absorption spectroscopy (MAX-DOAS), a well-established, unique, and
74 powerful remote sensing method for measuring trace gases and aerosols, is based on the DOAS technique.
75 Aerosols and trace gases are quantified using selective narrowband (high frequency) absorption features
76 (Platt 1994; Platt and Stutz 2008). Spectral radiance measurements at different elevation angles (ELs) can
77 provide profile information about atmospheric trace gases and aerosols (Hönninger et al., 2004; Wagner
78 et al., 2004; Wittrock et al., 2004; Frieß et al., 2006; Irie et al., 2008a). Many studies have demonstrated
79 the retrieval of aerosol and trace gas concentrations and profiles from MAX-DOAS observations,
80 including NO_2 and HCHO (Clémer et al., 2010; Irie et al., 2011; Hendrick et al., 2014; Wang et al., 2014;
81 Franco et al., 2015; Frieß et al., 2016).

82 The ability of MAX-DOAS to provide information related to surface concentrations, vertical profiles,
83 and column densities makes it a good complement to ground-based in situ and satellite observations.

Moreover, the MAX-DOAS method uses narrowband absorption of the target compounds, thereby obviating any need for radiometric calibration of the instrument. Because of these advantages, MAX-DOAS systems are deployed for the assessment of aerosol and trace gases in regional and global observational networks such as BREDOM (Wittrock et al., 2004), BIRA-IASB (Clémer et al., 2010), and MADRAS (Kanaya et al., 2014). Such datasets are used, in but are not limited to, (1) air quality assessment and monitoring, (2) evaluation of chemistry-transport models (CTMS), and (3) validation of satellite data retrievals. Several studies have used MAX-DOAS datasets to validate tropospheric columns retrieved from satellite observations, including NO₂ and HCHO (Irie et al., 2008b; Ma et al., 2013; Chan et al., 2020; Ryan et al., 2020). However, limited MAX-DOAS datasets have been used to evaluate global CTMs. Vigouroux et al. (2009) and Franco et al. (2015) respectively used the MAX-DOAS HCHO datasets from Reunion Island and Jungfraujoch stations to evaluate the Intermediate Model of Annual and Global Evolution of Species (IMAGES) and GEOS-Chem model simulations. Kanaya et al. (2014) validated the Model for Interdisciplinary Research on Climate–Earth System Model – Chemistry (MIROC-ESM-CHEM) simulated NO₂ column densities with MAX-DOAS observations in Cape Hedo and Fukue in Japan. Kumar et al. (2021) used MAX-DOAS observations to evaluate the high-resolution regional model Meco(n)(MESSy-field ECHAM and COSMO model nested n times).

For this study, NO₂ and HCHO profiles retrieved from MAX-DOAS observations from the International air quality and sky research remote sensing (A-SKY) (<http://atmos3.cr.chiba-u.jp/a-sky/>) network sites are used to evaluate the global Chemical Atmospheric General Circulation Model for the Study of Atmospheric Environment and Radiative Forcing (CTM CHASER; Sudo et al., 2002). The three A-SKY sites of - (1) Phimai in Thailand (15.18°N, 102.56°E), (2) Pantnagar (29°N, 78.90°E) in the IGP in India, and (3) Chiba (35.62°N, 140.10°E) in Japan, are respectively representative of rural, semi-rural, and urban environments. CHASER has been used mostly for global-scale research (Sudo et al., 2007; Sekiya et al., 2014, 2018; Miyazaki et al., 2017). The study described herein is the first reported attempt to evaluate the CHASER-simulated NO₂ and HCHO profiles using MAX-DOAS observations in three different atmospheric environments. Moreover, few reports of the literature have described the use of MAX-DOAS datasets to evaluate global CTMs in South Asia and South-east Asia. Overall, this study was conducted

111 to provide important insights into model performances and to help reduce model uncertainties related to
112 NO₂ and HCHO simulations in these regions.

113 The paper is structured in the following manner. First, the observation sites, MAX-DOAS
114 instrumentation, and retrieval strategies are described in section 2. Section 2 also includes a short
115 description of the CHASER model and Ozone Monitoring Instrument (OMI) HCHO and NO₂ retrievals.
116 Next, the observations and the evaluation results are described in sections 3. Finally, the sensitivity study
117 results are provided in section 3.4. and the concluding remarks in section 4.

118

119

120 2 Observations, datasets, and methods

121

122 2.1 Site Information

123 Continuous MAX-DOAS observations at Chiba, Phimai, and Pantnagar started respectively in 2012,
124 2014, and 2017. The measurements from January 2017 to December 2018 at all three sites are discussed
125 herein. Phimai, a rural site, is located ~260 km north-east of the Bangkok metropolitan area and is unlikely
126 to be affected by vehicular and industrial emissions. However, the site is affected by biomass burning
127 during January - April. Two major air streams: the dry, cool north-east monsoon during November – mid-
128 February and the wet, warm south-west monsoon during mid-May – September affect the climate in
129 Phimai. As described by, Hoque et al. (2018), the climate classifications of Phimai are the (a) dry season
130 (January – April), and (b) wet season (June – September).

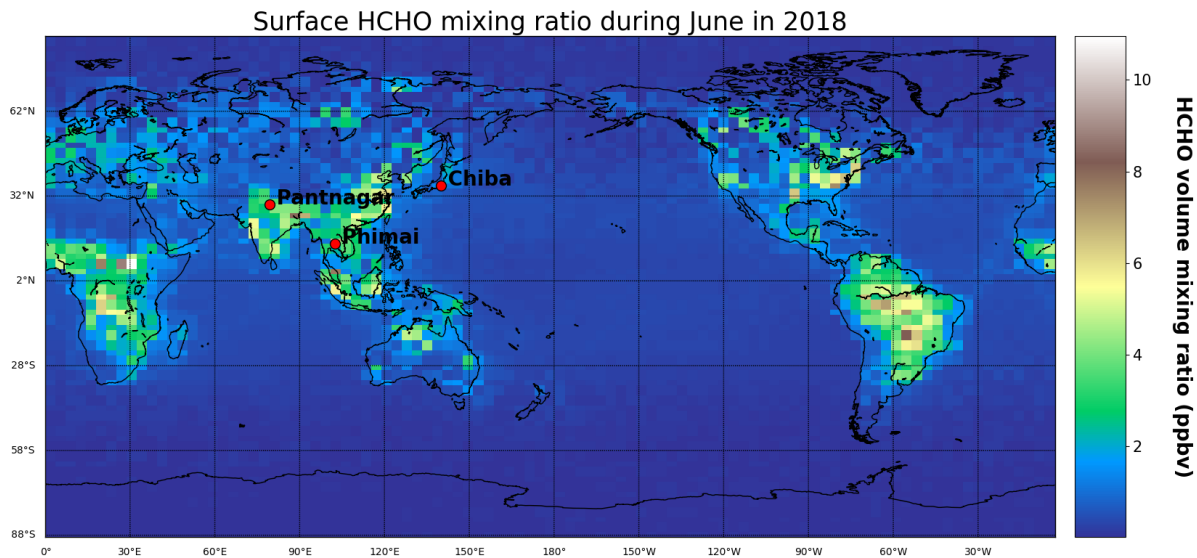
131 Pantnagar, a semi-urban site in India, is located in the IGP. The Indian capital of New Delhi is situated
132 at ~225 km south-west of the site. The low-altitude plains are on the south and west sides of the site. The
133 Himalayan mountains are located to the north and east. An important roadway with moderate traffic
134 volume and a small local airport lies within 3 km of the site. Rudrapur (~12 km south-west of Pantnagar)
135 and Haldwani (~ 25 km north-east of Pantnagar) are the two major cities near Pantnagar, where industries
136 (Fast moving Consumable Goods, electroplating, plywood, pharmaceuticals, automobile and allied
137 industries (Banerjee and Srivastava 2009)) are located. The climate classification at Pantnagar is the

138 following: (1) winter (December–February), (2) spring (March–May), (3) summer monsoon (June–
139 August), and (4) autumn (September–November).

140 Chiba, an urban site, is located ~40 km south-east of the Tokyo metropolitan region. Tokyo Bay,
141 large-scale industries, and residential areas are located within a 50 km radius. Chiba has four distinct
142 seasons: (1) spring (March–May), (2) summer (June–August), (3) autumn (September–November), and
143 winter (December– February). The locations of the three sites are depicted in Fig. 1.

144

145



146

147

148 **Figure 1:** Surface HCHO mixing ratio during June 2018, simulated using the CHASER model. The red
149 points represent locations of the observation sites, which are part of the A-SKY network.

150

151

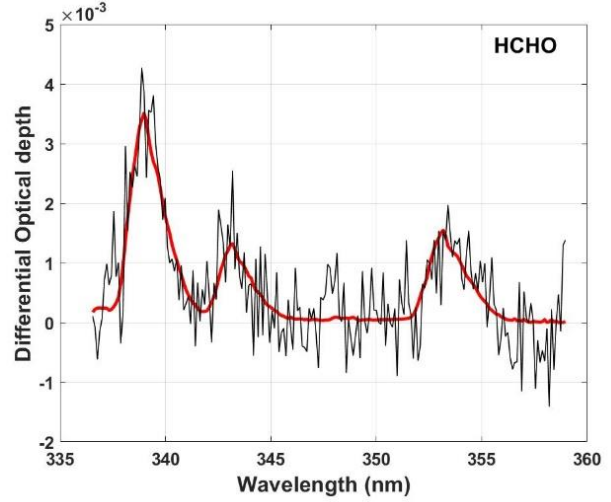
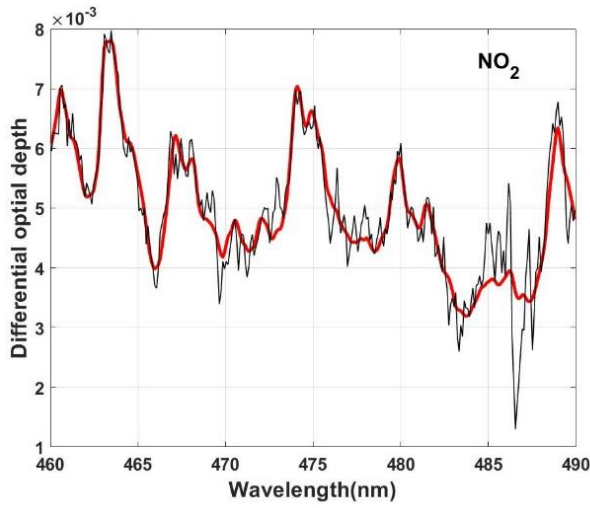
152 2.2 MAX-DOAS retrieval

153 The MAX-DOAS systems used for continuous observations at the three sites participated in the Cabauw
154 Intercomparison Campaign of Nitrogen Dioxide measuring Instruments (CINDI) (Roscoe et al., 2010)
155 and CINDI-2 (Kreher et al., 2020) campaigns. The instrumentation setup is described by Irie et al. (2008,
156 2011, 2015). The indoor part of the MAX-DOAS systems consists of an ultraviolet-visible (UV-VIS)
157 spectrometer (Maya2000Pro; Ocean Optics Inc.) embedded in a temperature-controlled box. The outdoor
158 unit consists of a single telescope and a 45° inclined movable mirror on a rotary actuator, used to perform
159 reference and off-axis measurements. The high-resolution spectra from 310–515 nm is recorded at six
160 elevation angles (ELs) of 2°, 3°, 4°, 6°, 8°, and 70° at the Chiba and Phimai sites. At the Pantnagar site,
161 measurements are conducted at ELs of 3°, 4°, 5°, 6°, 8°, and 70°. The sequences of the ELs at all the sites
162 were repeated every 15 min. The reference spectra are recorded at EL of 70° instead of 90° to avoid
163 saturation of intensity. Because all the ELs were considered in the box air mass factor (A_{box}) calculation
164 to retrieve the vertical profile, the choice of reference EL (70° or 90°) is not an important issue for this
165 study. The off-axis ELs are limited to < 10° to reduce the systematic error in the in-oxygen collision
166 complex (O_4) fitting results (Irie et al., 2015), thereby maintaining high sensitivity in the lowest layer of
167 the retrieved aerosol and trace gas profiles. Daily wavelength calibration using the high-resolution solar
168 spectrum from Kurucz et al. (1984) is performed to account for the spectrometer's long-term degradation.
169 The spectral resolution (full width half maximum: FWHM) is about 0.4 nm at 357 and 476 nm. The
170 concentrations and profiles of aerosol and trace gases are retrieved using the Japanese vertical profile
171 retrieval algorithm (JM2 ver. 2) (Irie et al., 2011, 2015). The algorithm works in three steps: (1) DOAS
172 fittings, (2) profile/column retrieval of aerosol, and (3) profile/column retrieval of trace gases. Irie et al.
173 (2008a, 2008b, 2011, 2015) described the retrieval procedures, and the error estimates. Herein we provide
174 a short overview.

175 First, the differential slant column density (Δ SCD) of trace gases is retrieved using the DOAS
176 technique (Platt 1994), which uses the nonlinear least-squares spectral fitting method, according to the
177 following equation :

$$\ln I(\lambda) = \ln(I_o(\lambda) - c(\lambda)) - \sum_i^n \sigma_i(\lambda) \Delta SCD_i - p(\lambda) \quad (1)$$

Therein, $I_o(\lambda)$ represents the reference spectrum measured at time t . $I_o(\lambda)$ is derived by interpolating two reference spectra (i.e., EL=70°) within 15 min before and after the complete sequential scan of the off-axis ELs at time t . ΔSCD represents the difference between the slant column density along the off-axis and reference spectrum. Second- and third-order polynomials are fitted to account, respectively, the wavelength-dependent offset $c(\lambda)$ and the effect of molecular and particle scattering $p(\lambda)$. In addition, $c(\lambda)$ accounts for the influence of stray light. The HCHO ΔSCD and NO₂ ΔSCD are retrieved respectively, from the fitting windows of 340–370 and 460–490 nm. Significant O₄ absorptions in the 338–370 and 460–490 nm fitting windows are used to retrieve the O₄ ΔSCD s. The absorption cross-section data sources and the fitted absorbers in the HCHO and NO₂ fitting windows are given in Table 1. Figure 2 presents an example of the fitting results. O₄ fittings in both retrieval windows are shown in Fig S1 (supplementary information).



191 **Figure 2:** Examples of spectral fitting of NO₂ and HCHO, where red and black lines **respectively** show the scaled
 192 cross-section and the summation of scaled cross-sections and fitting residuals, respectively. The example shows
 193 the measurements on 10 April 2017, **in Phimai** at 10:00 LT at an EL of 2°.

194 In the second step, the aerosol optical depth (AOD) τ and the vertical profiles of the aerosol extinction
 195 coefficient (AEC) k are retrieved **using the approach developed by Irie et al, (2008a) which is based on**
 196 **the optimal estimation method (Rogers, 2000).** In this approach, the measurement vector y (representing
 197 the quantities to be fitted) and state vector (representing the retrieved quantities) is defined as

198

$$199 \quad y = (O_4 \Delta SCD(\Omega_1) \dots \dots \Delta SCD(\Omega_n))^T \quad (2) \text{ and}$$

$$200 \quad x = (\tau F_1 F_2 F_3)^T \quad (3),$$

201

202

203 **Table 1.** Cross-section data references and absorbers fitted in the HCHO and NO₂ windows

Cross-section	Absorbers fitted	Data Source
O ₃		Bougmil et al. (2003), 223K
NO ₂	O ₃ , NO ₂ , H ₂ O, O ₄ , Ring	Vandaele et al. (1996), 295K
BrO		Fleischmann et al. (2004), 223K
Ring		Chance and Spurr (1997)
H ₂ O		Vandaele et al. (2005), 280K
O ₄		Hermans et al. (2003), 296K
HCHO	O ₃ , NO ₂ , HCHO, BrO, O ₄ , Ring	Meller and Moortgart (2000), 293k

204

205

206 where n stands for the number of measurements within one complete scan of an EL sequence. Also, Ω
207 denotes the viewing geometry and includes three components: solar zenith angle (SZA), EL, and relative
208 azimuth angle (RAA). The F values determine the profile shape, with values between 0 and 1. The partial
209 AOD for 0–1, 1–2, 2–3, and above 3 km layers were defined respectively as $AOD \cdot F_1$, $AOD \cdot (1-F_1) F_2$,
210 and $AOD \cdot (1-F_1) (1-F_2) F_3$, and $AOD \cdot (1-F_1) (1-F_2) (1-F_3)$. The AEC profile from 3 to 100 km is derived

211 assuming a fixed value at 100 km and exponential AEC profile shape with a scaling height of ~1.6 km.
 212 The k value at 100 km was estimated from Stratospheric Aerosol and Gas Experiment III (SAGE III)
 213 aerosol data ($\lambda=448$ and 521 nm) taken at altitudes of 15–40 km. The non-substantial influence of such
 214 assumptions on the retrievals in the lower troposphere has been demonstrated in sensitivity studies
 215 reported by Irie et al (2012). Similarly, the AEC profiles at 2–3, 1–2, and 0–1 km were derived. Such
 216 parameterization provides the advantage that the AEC profile can be retrieved using only the apriori
 217 knowledge of the F values (profile shape) and little or no information related to the absolute AEC values
 218 in the troposphere. Irie et al. (2008a) demonstrated that the relative variability of the profile shape, in
 219 terms of 1-km averages, is smaller than that of the absolute AEC values. AEC profile shapes
 220 corresponding to different F values is shown in Fig.S2 (supplementary information). However, the
 221 vertical resolution and the measurement sensitivity cannot be derived directly with such a
 222 parameterization (Irie et al., 2008a; 2009). The retrievals and simulations conducted by other groups for
 223 similar geometries (i.e., Frieß et al., 2006) are used to overcome such limitations. The apriori values used
 224 for this study were similar to those reported by Irie et al. (2011): $AOD = 0.21 \pm 3.0$, $F_1 = 0.60 \pm 0.05$, F_2
 225 $= 0.80 \pm 0.03$, and $F_3 = 0.80 \pm 0.03$.

226 Then, a lookup table (LUT) of the box air mass factor (A_{box}) vertical profile at 357 and 476 nm is
 227 constructed using the radiative transfer model JACOSPAR (Irie et al., 2015), which is based on the Monte
 228 Carlo Atmospheric Radiative Transfer Simulator (MCARaTS) (Iwabuchi, 2006). The values of the single-
 229 scattering albedo (s), asymmetry parameter (g), and surface albedo were, respectively, 0.95, 0.65 (under
 230 the Henyey-Greenstein approximation), and 0.10. The U.S. standard atmosphere temperature and pressure
 231 profiles were used for radiative transfer calculations. Uncertainty of less than 8% related to the usage of
 232 fixed values of s , g , and a were estimated from sensitivity studies (i.e., Irie et al 2012). Results obtained
 233 from JACOSPAR are validated in the study reported by Wagner et al. (2007). The optimal aerosol load
 234 and the A_{box} profiles are derived using the A_{box} LUT and the O_4 Δ SCD at all ELs.

235 In the third step, the A_{box} profiles, HCHO and NO_2 Δ SCDs, and the nonlinear iterative inversion
 236 method are used to retrieve the HCHO and NO_2 vertical column densities (VCDs) and profiles. Here the
 237 NO_2 retrieval is explained.

238

For trace gas retrieval, the measurement vector and state vector are defined as

$$y = (NO_2\Delta SCD(\Omega_1) \dots \dots NO_2\Delta SCD(\Omega_n))^T \quad (4) \text{ and}$$

$$x = (VCD f_1 f_2 f_3)^T \quad (5)$$

VCD represents the vertical column density below 5 km. The f values are the profile shape factors. Above the 5 km layer, fixed profiles are assumed. Similarly, to aerosol retrieval, the partial VCD values for the 0–1, 1–2, 2–3, and 3–5 km is defined respectively as $VCD \cdot f_1$, $VCD \cdot (1-f_1) f_2$, $VCD \cdot (1-f_1) (1-f_2) f_3$, and $VCD \cdot (1-f_1) (1-f_2) (1-f_3)$. Finally, the volume mixing ratio (VMR) is calculated using the partial VCD, and U.S. standard atmosphere temperature and pressure data scaled to the respective surface measurements.

The calculated vertical profile is converted to $NO_2 \Delta SCDs$ using the A_{box} LUT constructed for aerosol retrieval. However, the trace gas wavelengths differed from the representative wavelengths of A_{box} LUT (357 and 476 nm). Therefore, the AOD at the trace gas wavelength is estimated, converting the retrieved AOD to the closer aerosol wavelength of 357 or 476 nm, assuming the Angstrom exponent value of 1.00. The choice of the Angstrom exponent value can induce uncertainty in the retrieved VCDs. However, such uncertainty was found to be non-significant compared to that of A_{box} profiles. Uncertainty in the A_{box} profiles are assumed to as high as 30 to 50%. Such values are derived empirically from comparison with sky radiometer and LIDAR observations (i.e., Irie et al., 2008b). Then, the A_{box} profiles from the LUT corresponding to the recalculated AOD values are selected. The dependence of the A_{box} profiles on the concentration profiles is expected to be low because both HCHO and NO_2 are optically thin absorbers (Wagner et al., 2007; Irie et al., 2011). For every 15 min (time necessary for one complete scan of ELs), 20% (the mean ratio of the retrieved VCD to maximum ΔSCD) of the maximum trace gas $\Delta SCDs$ is used as a priori information for the VCD retrievals. The a priori error is set to 100% of the maximum trace gas ΔSCD . Figure 3 presents the mean averaging kernel (AK) of the HCHO and NO_2 retrievals during the dry season at Phimai. The area (Rodgers, 2000) provides an estimate of the measurement contribution to the retrieval. The total area is the sum of all the elements in the AK and weighted by the a priori error (Irie et al. 2008a). The areas for VCD and f_1 of NO_2 retrieval are 1 and 0.6, respectively. The f_2 and f_3 values are much smaller. Consequently, at first, the a priori profiles were scaled, and later f values determined

the profile shape. The VCD area is close to unity, and therefore, the retrieved VCD is independent of the a priori values. Irie et al (2008) conducted sensitivity studies of choice of the f values and reported negligible effect on the retrievals.

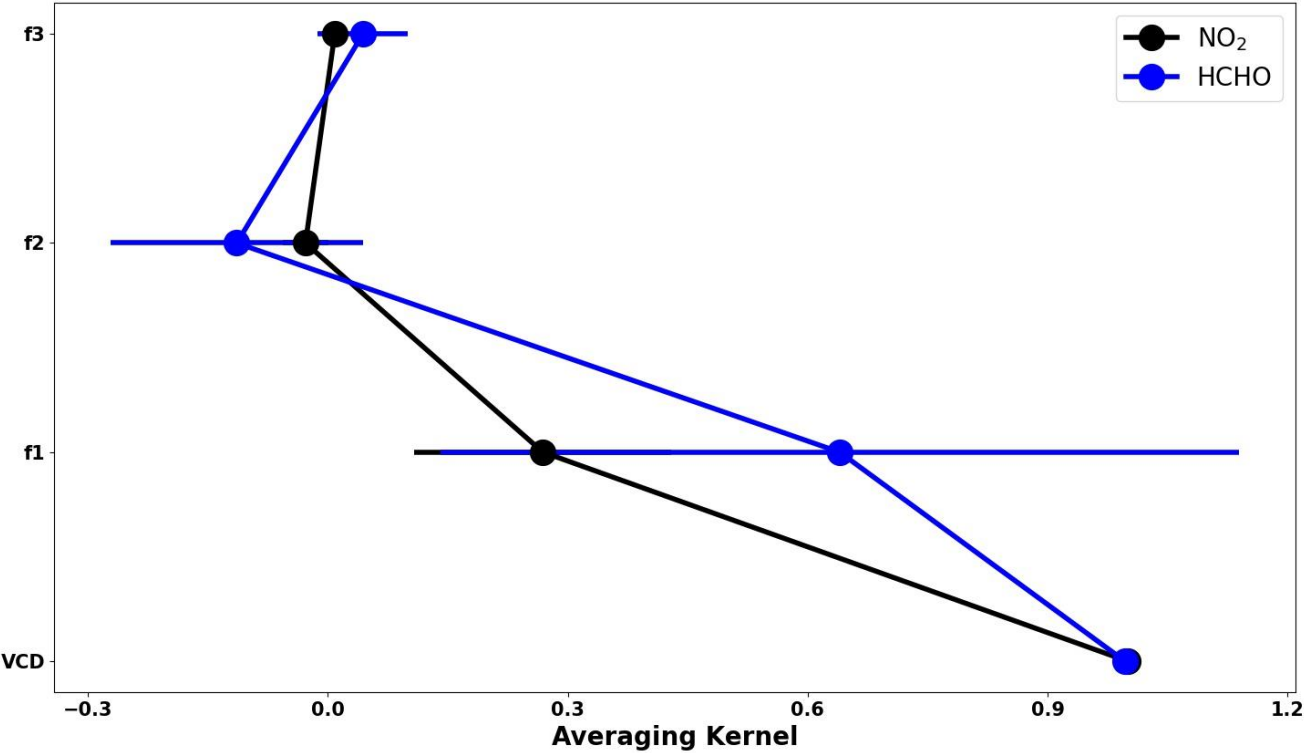


Figure 3: Mean averaging kernel of the NO₂ and HCHO retrievals from observations at Phimai during 2017

The total error of the retrieval consists of random and systematic errors. The measurement error covariance matrix constructed from the residuals of the respective trace gas Δ SCDs is used to estimate the random error. The systematic error is calculated while assuming uncertainties as high as 30 and 50% in the retrieved AOD (or the corresponding A_{box} values). Table 2 shows the total estimated error. Aside from the random and systematic error, more sources of error might exist. For instance, the bias in the ELs can induce uncertainties in the retrieved products. However, Hoque et al. (2018) demonstrated that such biases had a non-significant effect on the final retrieved products, mostly less than 5%.

281 The cloud screening procedure is similar to that described by Irie et al. (2011) and by Hoque et al.
 282 (2018a, 2018b). During the retrieval steps, retrieved AOD values greater than 3 are excluded, because
 283 optically thick clouds are primarily responsible for such large optical depth. Filtering based on the
 284 residuals of O₄ and the trace gas ΔSCDs is also used to screen clouds. The screening criteria are: respective
 285 residuals of O₄, HCHO, and NO₂ ΔSCDs < 10%, < 50%, and <20%, and the degrees of freedom of
 286 retrievals greater than 1.02. The threshold values were determined statistically corresponding to the mode
 287 plus one sigma (1σ) in the logarithmic histogram of relative residuals.

288
 289 **Table 2.** Estimated Errors (%) for the NO₂ and HCHO concentration in 0-1 km layer, retrieved using the
 290 JM2 algorithm

Retrieved Product	Random error	Systematic error	Error related to instrumentation	Total error
NO ₂	10	12	5	16
HCHO	16	25	5	30

291
 292

293 **2.3 CHASER simulations**

294 CHASER 4.0 (Version 4) (Sudo et al., 2002; Sudo and Akimoto, 2007; Sekiya and Sudo, 2014), coupled
 295 online with the MIROC-AGCM atmospheric general circulation model (AGCM) (K-1 model developers,
 296 2004) and the SPRINTARS aerosol transport model (Takemura et al., 2005, 2009), is a global chemistry
 297 transport model used to study the atmospheric environment and radiative forcing. In addition, several
 298 updates, including the introduction of aerosol species (sulfate, nitrate, etc.) and related chemistry,
 299 radiation, and cloud processes, have been implemented in the latest version of CHASER.

300 CHASER can calculate the concentrations of 92 species through 263 chemical reactions (gaseous,
 301 aqueous, and heterogeneous chemical reactions) considering the chemical cycle of O₃–HO_x–NO_x–CH₄–
 302 CO along with oxidation of non-methane volatile organic compounds (NMVOCs)(Miyazaki et al., 2017).
 303 The chemical mechanism is largely based on the master chemical mechanism (MCM,

304 <http://mcm.york.ac.uk>(Jenkin et al., 2015). CHASER simulates the stratospheric O₃ chemistry
 305 considering the Chapman mechanisms, catalytic reactions related to halogen oxides (HO_x, NO_x, ClO_x,
 306 and BrO_x), and polar stratospheric clouds (PSCs). Resistance-based parameterization (Wesely, 1989),
 307 cumulus convection, and large-scale condensation parameterizations are used to calculate dry and wet
 308 depositions. The piecewise parabolic method (Colella and Woodward, 1984)
 309

310 **Table 3:** Settings of the CHASER simulations used in this study

Simulation	Anthropogenic emissions	Pyrogenic emissions	Biogenic emissions	Soil NO _x emission	Other physical and chemical processes
Standard	ON	ON	ON	ON	ON
L1_HCHO	ON	Pyrogenic VOCs switched	ON	ON	ON
L1_opt	ON	OFF	Reduced by 50%	ON	ON
L1_NO2	ON	ON	ON	OFF	ON
L2	Anthropogenic VOC emissions switched OFF	ON	ON	ON	ON

311
312 and the flux-form semi-Lagrangian schemes (Lin and Rood, 1996) calculate advective tracer transport.
313 CHASER simulates tracer transport on a sub-grid scale in the framework of the prognostic Arakawa–
314 Schubert cumulus convection scheme (Emori et al., 2001) and the vertical diffusion scheme (Mellor and
315 Yamada, 1974). In this study, CHASER simulations were conducted at a horizontal resolution of $2.8^\circ \times$
316 2.8° , with 36 vertical layers from the surface to ~50 km altitude and a typical time step of 20 min. The
317 meteorological fields simulated by MIROC-AGCM were nudged toward the six-hourly NCEP FNL
318 reanalysis data at every model time step.

319 The anthropogenic, biomass burning, lightning, and soil emissions of NO_x were incorporated into
320 CHASER simulations. Anthropogenic emissions were based on HTAP_v2.2 for 2008. Biomass burning
321 and soil emissions from the ECMWF/MAC (Global Fire Assimilation System (GFAS)) reanalysis were
322 used. The biogenic emissions for VOCs are based on the process-based biogeochemical model the
323 Vegetation Integrative SIMulator for Trace gases (VISIT) (Ito and Inatomi, 2012) simulations. The NO_x
324 production from lightning is calculated based on the parameterization of Price and Rind (1992) linked to
325 the convection scheme of the AGCM (Sudo et al., 2002). Isoprene, terpene, acetone, and ONMV
326 emissions estimates in the VISIT inventory during July were 2.14×10^{-11} , 4.43×10^{-12} , 1.60×10^{-12} , and
327 $9.93 \times 10^{-13} \text{ kgCm}^{-2}\text{s}^{-1}$. Global NO_x emissions of 43.80 TgNyr^{-1} are used in the simulations, considering
328 industries (23.10 TgNyr^{-1}), biomass burning (9.65 TgNyr^{-1}), soil (5.50 TgNyr^{-1}), lightning (5 TgNyr^{-1}),
329 and aircrafts (0.55 TgNyr^{-1}) as significant sources. Global isoprene emissions from vegetation were set to
330 400 TgCyr^{-1} .

331 NO_x emissions in India were estimated as 14 Tg/yr in 2016, almost two-fold increase since 2005 (~8
332 Tg/yr), with the energy and transportation sector being the largest contributor (Sadavarte et al 2014).
333 Indian anthropogenic non-methane VOCs (NMVOCs) emissions in 2010 were estimated ~ 10 Tg/yr ,
334 with respective contributions of 60, 16, and 12% from residential, solvents, and the transport sector(
335 Sharma et al 2015). In Japan, vehicular exhausts (14 - 25%), gasoline vapor (9 - 16%), liquefied natural
336 gas (7 - 10%), and liquefied petroleum gas (49 - 71%) contribute to the total VOC concentrations (Morino

et al., 2011), with annual NMVOC emission of ~2 Tg (Kannari et al., 2007). Annual NO_x emissions in Japan and Thailand in 2000 was estimated as ~2000 and 591 kt/yr, with the largest contribution from transport-oil use, followed by the energy and industrial sector (Ohara et al., 2007). Annual anthropogenic VOC emissions in Thailand are approximately 0.9 Tg, with 43, 38, and 20% contributed, respectively, from industrial, residential and transportation sectors (Woo et al; 2020).

Multiple CHASER simulations with different settings used for sensitivity studies are presented in Table 3.

2.4 Satellite observations

Tropospheric NO₂ and HCHO retrievals from the Ozone monitoring Instrument (OMI) were also used to evaluate the model simulations. The ultra-violet nadir-viewing spectrometer OMI, on board the Aura satellite measures backscattering solar radiation covering the spectral range of 270 – 500 nm (Levelt et al., 2006). In an ascending sun-synchronous polar-orbit, OMI crosses the equator at 13:40 LT (local time) (Zara et al., 2018). OMI measures at a spatial resolution of 13 × 24 km² and provides daily global coverage of various trace gases including NO₂ and HCHO. The NO₂ and HCHO datasets were obtained respectively from the TEMIS (www.temis.nl, last accessed on 2022/04/23) and aeronomie (<https://h2co.aeronomie.be/>, last accessed 2022/05/03) websites. For analysis, NO₂ tropospheric columns retrieved using the DOMINO version 2.0 (Boersma et al., 2011) algorithm were used for the analysis. Data meeting the following criteria were selected: cloud fraction < 0.5, SZA < 70°, surface albedo < 0.3, quality flags =0, and cross-track quality flags= 0. For HCHO, we used the BIRA-IASB v14 (De Smedt et al 2015) retrieved products. The data filtering criteria was the following: cloud fraction < 0.4, SZA<70°, AMF > 0.2, quality flag=0, and cross-track quality flag =0.

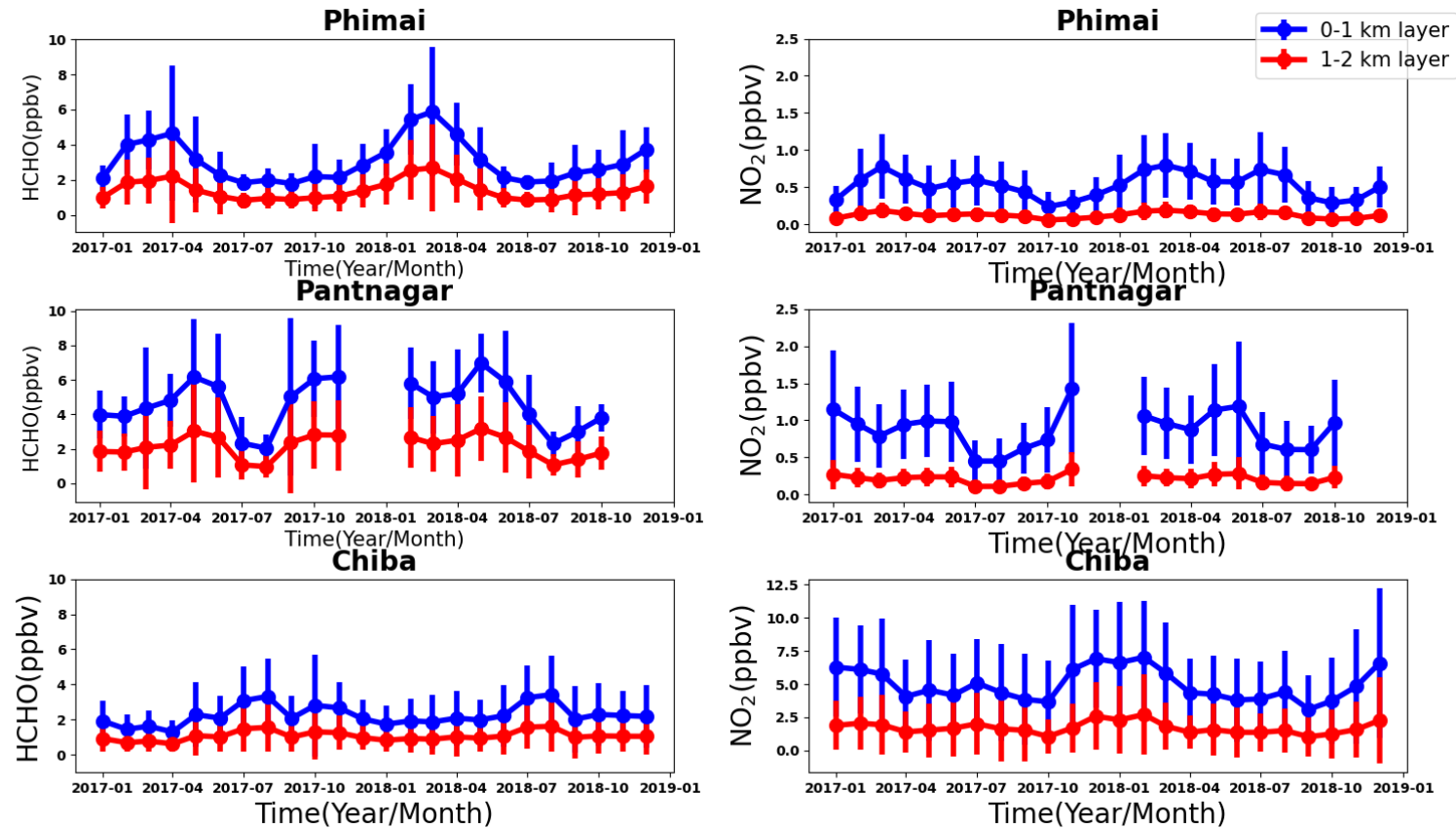
3 Results and discussion

3.1 Results from MAX-DOAS observations

363 **3.1.1 HCHO seasonal variation**

364 The monthly mean HCHO **mixing ratios** in the 0–1 and 0–2 km layers from January 2017 – December
365 2018 and **the corresponding one sigma (1σ) standard deviations signifying the variation ranges** for the
366 three sites are presented in Fig. 4. The HCHO levels at the Phimai site show a consistent seasonal cycle,
367 characterized by high **VMRs** during the dry season. Such enhancement is related to the influence of
368 biomass burning during the dry season, which has been well documented in the work of Hoque et al.
369 (2018). The HCHO **mixing ratio** at Phimai **reach a** peak in March or April, with a maximum of 4 – 6
370 ppbv. The variation in the peak concentration and timing **depends mainly** on the intensity of biomass
371 burning activities. During the wet season, the HCHO concentrations are mostly within 2–3 ppbv,
372 indicating a two-fold increase in HCHO abundances during the dry season. The daily mean HCHO
373 amounts (0–1 km) are 0.78 - 9.84 ppbv, representing seasonal modulation of 134%.

374



375 **Figure 4:** Seasonal variations in the HCHO (left panel) and NO₂ (right panel) mixing ratios in the 0 - 1 (blue) and
376 1 - 2 (red) km layers at Phimai, Pantnagar, and Chiba. The error bars represent the one sigma standard deviation of
377 the mean values. The gaps in the plots for the Pantnagar site indicate the unavailability of observations during the
378 investigated period.

379

380

381 Seasonal variation of HCHO in the 0–1 km layer at the Pantnagar site has been elucidated by Hoque
382 et al. (2018b). Here, the results are replotted to verify the consistency of the seasonal variations.
383 Observations made during autumn 2018 were not available because of problem with the spectrometer.
384 Consistent seasonal variation of HCHO abundances is observed at the Pantnagar site, with enhanced
385 concentrations during the spring. The Pantnagar site is affected by biomass burning during spring and
386 autumn (Hoque et al., 2018b), explaining the high mixing ratios found during spring. In both years, the
387 maximum HCHO mixing ratios are ~6 ppbv. The springtime peak occurred in May. The HCHO
388 concentrations during the monsoon are ~35% lower than in the spring, indicating a strong effect of the
389 monsoon on the HCHO concentrations found for Pantnagar. The seasonal modulation of HCHO at
390 Pantnagar estimated from the daily mean concentrations is 107%. The peak HCHO mixing ratio at
391 Pantnagar is almost twice that of in Pune city (~ 3 ppbv) (Biswas and Mahajan, 2021), a site in the IGP
392 region. The HCHO seasonality at the two sites are found to be dissimilar, because of differences in the
393 VOC sources, however, lower mixing ratios during the monsoon is consistent. From another site in the
394 IGP region (i.e., Mohali), Kumar et al., (2020) reported lowest HCHO VCDs during March 2014 and
395 2015, attributing them to lower biogenic and anthropogenic VOC emissions. At Pantnagar, the lowest
396 HCHO mixing ratios are observed during the monsoon. The rainfall events in the IGP region shows strong
397 annual variability (Fukushima et al. 2019). Discrepancies between the sites might be related to the rainfall
398 pattern.

399 Under the influence of biomass burning, the maximum monthly HCHO mixing ratios at Phimai and
400 Pantnagar are similar (~6 ppb). The maximum instantaneous HCHO VMR during biomass burning
401 influence in Phimai and Pantnagar are, respectively, 26 and 30 ppbv. Zarzana et al. (2017) reported HCHO
402 abundances of ~60 ppbv in fresh biomass plumes in the US. The lower values obtained from our

403 measurements might be attributable to (1) more aged plumes intercepted by the MAX-DOAS instruments
404 and (2) differences in the types of biomass fuel used. Comparison to reports of literature indicates that the
405 retrieval of HCHO under biomass burning is reasonable.

406 The summertime maximum and wintertime minimum characterize the seasonal variations of HCHO at
407 the Chiba site, with a peak at ~3 ppbv. The HCHO concentrations are ~2 ppbv during other seasons,
408 which are similar to the HCHO concentrations in Phimai during the wet season. The seasonal variation
409 amplitudes of HCHO at Chiba is ~94%. For a site with similar seasonal variation (i.e., summertime
410 maximum and wintertime minimum), Franco et al. (2015) reported HCHO seasonal modulation of 88%.

411 The HCHO VMRs in the 1–2 km layers at all three sites are lower, almost 50% the value of the
412 concentrations in the 0–1 km layer. The HCHO seasonal variation amplitudes at Phimai, Pantnagar, and
413 Chiba sites are, respectively, 131%, 102%, and 90% when calculated based on the HCHO concentration
414 in the 1–2 km layers. The modulation was even lower when retrieved values for the 2–3 km layer is used.

415 3.1.2 NO₂ seasonal variation at the three sites

416 Figure 4 also shows the seasonal variation of NO₂ in the 0–1 and 1–2 km layers at the three sites. The
417 error bars represent the 1 σ standard deviation of the mean values. The NO₂ seasonal variations at Phimai
418 and Pantnagar sites are similar to those of HCHO. Pronounced peaks attributable to biomass burning
419 influence is observed during the dry season at Phimai (~0.8 ppbv) and during spring (1.2 ppbv), and post-
420 monsoon (1.4 ppbv) at Pantnagar. The lowest NO₂ mixing ratios at Phimai and Pantnagar are, respectively,
421 ~0.2 and 0.5 ppbv. The NO₂ VMRs at Chiba is higher (~7 ppbv) during winter. The longer lifetime of
422 NO_x and lower NO/NO₂ ratio because of lower photochemical activity in winter lead to high NO₂ mixing
423 ratios at Chiba (Irie et al., 2021).

424 At Phimai, the NO₂ mixing ratios in both seasons are similar. However, when Hoque et al. (2018a)
425 reported the seasonal variations in NO₂ at Phimai during 2015 – 2018, the dry season mixing ratios were
426 higher. Table 4 shows the number of fire events during the dry seasons during 2015 - 2018. The fire data
427 are extracted from the MODIS Active Fire Detections database (<https://firms.modaps.eosdis.nasa.gov>,
428 last accessed on 2021/12/15). Data fulfilling the following criteria were chosen – (a) data points located
429 within 100 km of the Phimai site, (b) confidence of the data greater than 70%, and (c) observations during
430 the daytime. The lower fire counts during 2017 - 2018 compared to those of 2015 - 2016 period coincide

431 with the lower NO₂ levels in the former. Fire counts varied between 2017 and 2018 but did not affect the
432 NO₂ levels. However, HCHO levels changed with the number of fire occurrences between 2015 – 2018
433 (i.e., Figure 4 and Hoque et al.,2018a).

434 At such low NO₂ levels at Phimai, soil NO_x emissions are likely to make a greater contribution to
435 NO₂. Although NO₂ is not emitted directly from soils, biological processes emit NO, which is rapidly
436 converted to NO₂ (Hall et al., 1996). In addition, many studies have established a relation between soil
437 moisture and NO emissions (Carden et al., 1993; Zheng et al., 2000; Schindlbacher et al., 2004; Huber et
438 al., 2020). The potential contribution of soil NO_x emissions, as inferred from CHASER simulations, is
439 discussed in section 3.4.2.

440 **Table 4:** Number of fire events occurring during the dry season (January - April) at Phimai from 2015
441 - 2018. Selection criteria of the data are the following: (1) situated within 100 km of the site, (2)
442 confidence level > 70%, and (c) daytime measurements.

Dry season years	Number of fire events
2015	84
2016	98
2017	62
2018	77

443

444

445 **3.1.3.1 The HCHO to NO₂ ratio (R_{FN}):**

446 The HCHO to NO₂ (R_{FN}) ratio is regarded as an indicator of high ozone O₃ sensitivity (Martin et al., 2004;
447 Duncan et al., 2010). The O₃ production regime is characterized as VOC-limited for $R_{FN} < 1$ and NO_x-
448 limited when $R_{FN} > 2$, and the values in the range 1-2 are said to be in the transition/ambiguous region
449 (Duncan et al., 2010; Ryan et al., 2020). Subsequent to a report of Tonnesen and Dennis (2000), several
450 studies used R_{FN} estimated from satellite and ground-based observations to infer O₃ sensitivity to NO_x
451 and VOCs (Martian et al., 2004; Duncan et al., 2010; Jin and Holloway et al.,2015; Mahajan et al., 2015;
452 Irie et al.,2021; etc.). However, the effectiveness of R_{FN} is still under discussion primarily based on two-
453 points- (1) the range of the transition region to categorize the VOC and NO_x -limited region, and (2) the

altitude dependence of R_{FN} (Jin et al., 2017). Most of the studies described above used the transition range ($1 < R_{FN} < 2$) proposed by Duncan et al. (2010). Schroeder et al. (2017) reported that a common transition (i.e., $1 < R_{FN} < 2$) range might not be valid globally. Instead, it should be calculated based on the region. First, the results based on the standard transition range are discussed herein, and then its applicability to the study regions is assessed.

Figure 5 shows scatter plots of the daily mean NO_2 and HCHO concentrations in the 0 - 2 km layer at the three sites, color-coded with the respective O_3 concentrations (0-2 km). Retrieval of the JM2 O_3 product is explained by Irie et al. (2011). The O_3 concentrations for $\text{SZA} < 50^\circ$ are used to minimize stratospheric effects. The JM2 O_3 product showed good agreement with ozonesonde measurements (Irie et al., 2021). Most of the high O_3 occurrences fall in the $R_{FN} > 2$ region at Phimai and Pantnagar and in $R_{FN} < 1$ at Chiba. The common transition range classifies the O_3 production regime as NO_x -limited at Phimai and Pantnagar and VOC-limited at Chiba. At all sites, the R_{FN} values tend to be biased to a particular regime (i.e., NO_x - or VOC-limited), with only 4 and 2% of the ratios in the range 0 - 2, at Phimai and Pantnagar, respectively. This finding suggests that the transition occurs at a higher or lower ratio than the common definition. Recent report by Sourì et al. (2020) found that the NO_2 - HCHO relation plays an important role in determining the transition region and derived a formulation from accounting for the NO_2 - HCHO chemical feedback in the ratios as

$$HCHO = m * (NO_2 - b) \quad (6)$$

where m and b respectively denote the slope and intercept. Equation (6) is based on observations, which means that the regionally adjusted fitting coefficients will reflect the local NO_2 - HCHO relation. Solving equation (6), the transition line estimated from the observations in the 0 - 2 km layer, is shown in Fig 5 (bottom panel). Rather than a range, the method calculates a single transition line, which corresponds to the NO_2 - HCHO feedback. The regions above and below the transition line are characterized, respectively as VOC- and NO_x -limited or other.

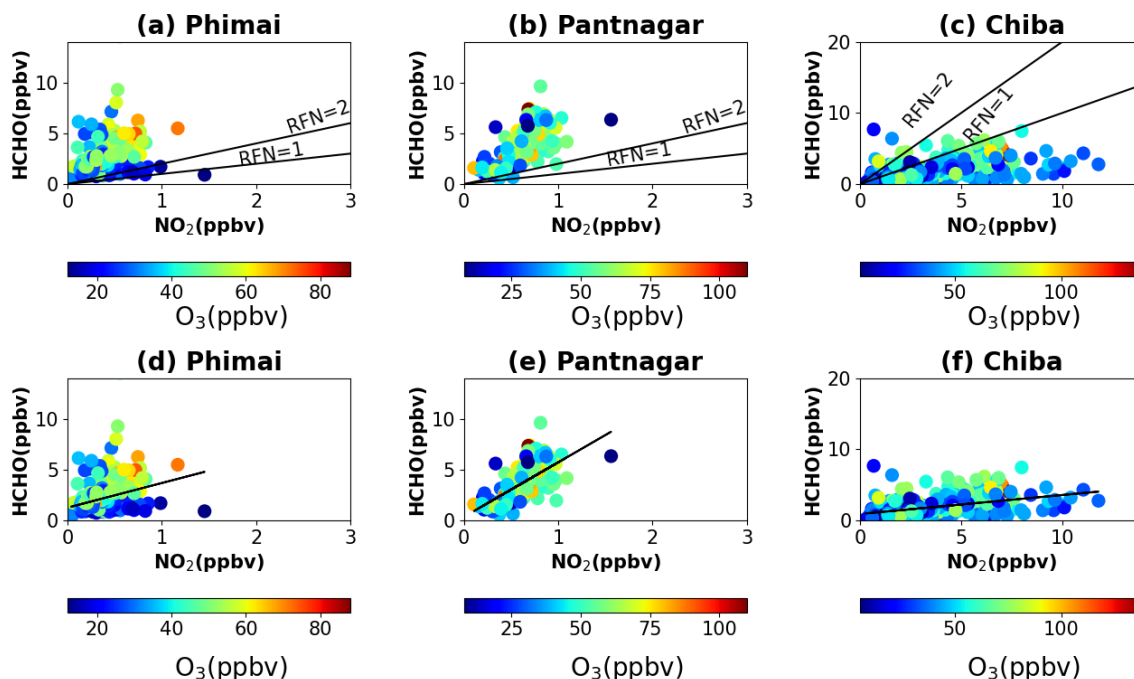


Figure 5. Scatter plots of HCHO and NO₂ concentrations in the 0-2 km layer at (a, d) Phimai, (b, e) Pantnagar, and (c, f) Chiba, coloured with the O₃ concentrations in the 0-2 km layer at the respective sites. The solid lines in the top panel represent $R_{FN} = 2$ and $R_{FN} = 1$ benchmarks. The black lines in the bottom panel are calculated according to equation (1).

The revised transition line at Phimai and Pantnagar is apparently more reasonable than the earlier method. At Phimai, the transition line almost clearly distinguishes between the high and low O₃ occurrences. It is perceptible that when the HCHO concentrations are higher than NO₂, the transition of the regimes is likely to occur at higher R_{FN} values. The minimum and mean R_{FN} value along the transition line are 3.62 and 6.78, respectively. Because Phimai is a VOC-rich environment, the regime transition occurs at higher R_{FN} values than by the conventional definition. This finding echoes the results reported by Schroder et al. (2017) for a regionally variable transition region. The definition of $R_{FN} < 1$ as a VOC-limited regime might not be valid in this case. Considering the mean R_{FN} ratio along the transition line (i.e., 6.78), the VOC-

492 and NO_x -limited (and other) regimes are defined, respectively as $R_{FN} < 6.78$ and $R_{FN} > 6.78$. Based on this
493 definition, around 34% (65%) of the ratios are higher (lower) than 6.78, classifying Phimai as a dominant
494 VOC-limited region, which contradicts earlier results. Biomass burning affects Phimai during January -
495 April and is a significant emission source in addition to biogenic emissions. Thus, high O_3 occurrences
496 likely occur only 30% of the time during a year. Such events mostly lie above the transition line.
497 At Pantnagar, high O_3 occurrences lie below (42%) and above (57%) the transition line, indicating that
498 O_3 production is sensitive to both HCHO and NO_2 which contradicts results reported by Biswas et al.
499 (2019). Based on satellite and ground-based observations, the study estimated the R_{FN} values at a site in
500 the IGP as > 4 and > 2 respectively, and regarded the O_3 regime as NO_x -limited. Mahajan et al (2015)
501 reported R_{FN} values of less than 1 over the IGP region signifying as a VOC-limited region. Pantnagar is
502 a sub-urban site situated beside a busy road. Therefore, effects of anthropogenic emissions are expected
503 year-round, especially with pyrogenic emissions during the spring and post-monsoon period. O_3
504 sensitivity to both NO_x and VOCs in the north-west IGP region has also been reported by Kumar and
505 Sinha (2021). Therefore, the balance between the VOC and NO_x -limited region in the IGP is reasonable.
506 The mean and minimum R_{FN} value along the transition line are, respectively, 5.59 and 6.09. The minimum
507 value (i.e., 5.59) is higher than Phimai (3.26), suggesting higher VOC levels at Pantnagar, consistent with
508 the observations.

509 At Chiba, 60% of the R_{FN} values lie below the transition line, suggesting a dominant VOC-limited
510 region, which is consistent with the results reported by Irie et al. (2021). The minimum and the mean R_{FN}
511 along the transition line are, respectively, 0.33 and 0.72. The transition occurs at a low R_{FN} value because
512 of higher NO_2 levels. The fact that, 40% of the R_{FN} values are above the transition region suggests a
513 moderate effect of HCHO on the O_3 sensitivity at Chiba.

514 Although the new classification results are apparently reasonable, they should be interpreted with
515 care. Our current understanding of R_{FN} contradicts the classification of rural sites as VOC-limited. Despite
516 the theoretical and observational evidence (i.e., Souri et al., 2020), the classification of regimes based on
517 a single transition line is not yet well-established. Schroder et al. (2017) used regionally varying transition
518 ranges. Moreover, (a) the number of observations and (b) the systematic and retrieval errors can affect
519 the estimations and classifications. These findings are expected to contribute to the ongoing discussion

520 about the effectiveness of R_{FN} . However, the results support the idea of a regionally varying transition
521 range.

522

523 3.1.3.2 R_{FN} profiles

524 Figure 6 shows the seasonal mean R_{FN} profiles at the three sites. Only the profiles during the high O_3
525 concentrations at the sites (i.e., March at Phimai, May at Pantnagar, and February at Chiba) are shown.
526 The R_{FN} values are likely increase with height because of the lower vertical gradient of NO_2 , than that of
527 HCHO (Fig.4). It is particularly interesting that, the R_{FN} values are similar in the 1-2 km height under
528 biomass burning conditions, suggesting a small variation in the HCHO loss rate in the particular layer. At
529 both sites, the HCHO concentration at 1.5 km is about 3 ppbv. At Chiba, a considerable amount of NO_2
530 in the higher layers increases the ratio up to 2 km height. Beyond 2 km, the ratio variation at all sites is
531 opposite that found for the surface. The gradient issue of R_{FN} has been discussed explicitly by Jin et al.
532 (2017). They proposed a conversion factor to account for gradient differences in the surface and column-
533 derived R_{FN} values, estimating the conversion factor from the model simulated surface and column
534 abundances of NO_2 and HCHO. We adopt the method reported by Jin et al. (2017) for this study using
535 the CHASER simulated NO_2 and HCHO concentrations and vertical columns.

536 First, CHASER simulated near-surface NO_2 and HCHO concentrations were converted to number
537 density. The effective boundary layer height (E) (Halla et al., 2011; Jin et al., 2017) was estimated.

538

$$539 \quad E_{NO_2} = \frac{NO_2 \text{ total column}}{NO_2 \text{ near-surface number density}} \quad (7)$$

540

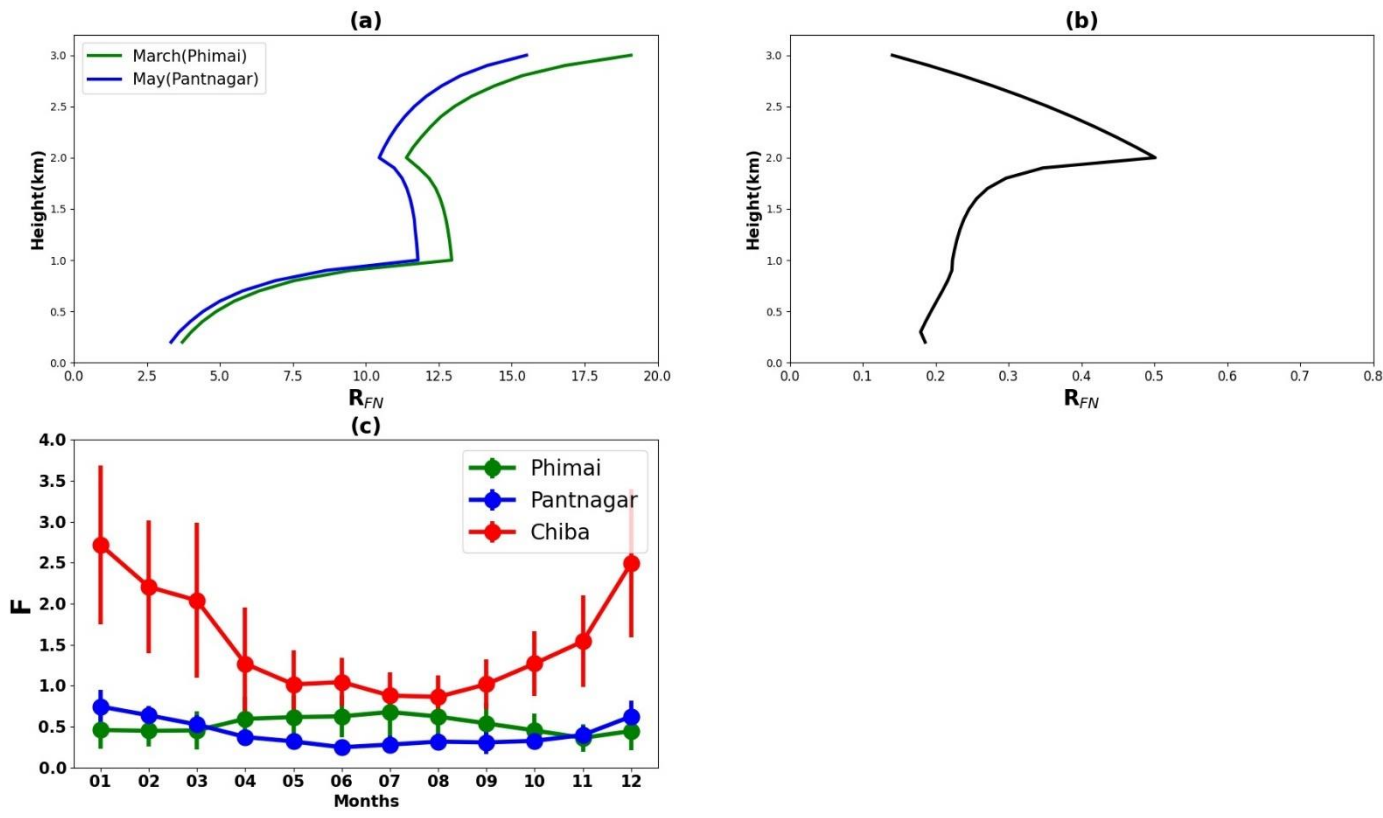
$$541 \quad E_{HCHO} = \frac{HCHO \text{ total column}}{HCHO \text{ near-surface number density}} \quad (8)$$

542 Therein, E_{NO_2} and E_{HCHO} respectively denote the effective boundary layer heights of NO_2 and HCHO.

543 In the second step, the column to surface conversion factor (F) was calculated according to the following
544 equation:

$$545 \quad F = \frac{E_{HCHO}}{E_{NO_2}} \quad (9)$$

546 The seasonal variation of F for the three A-SKY sites and the associated 1σ standard deviation of the
 547 mean values are depicted in Fig. 7(c). The F values over East Asia reported by Jin et al. (2017) were ~ 2 ,
 548 without marked seasonal variation. CHASER estimated F values over Chiba range between 1–2.5, which
 549 is apparently reasonable, when compared with literature values. Values reported in literature for polluted
 550 regions ($\text{NO}_2 > 2.5 \text{ molecules cm}^{-2}$) considered simulation data for 1–2 PM, but the estimates for this
 551 study used daytime (07:00 – 18:00) simulations.



552
 553 **Figure 6:** Seasonal mean R_{FN} profiles during (a) March and May at Phimai and Pantnagar, respectively, and (b)
 554 February at Chiba. (c) Seasonal variations in the column to surface conversion factor (F) for the Phimai, Pantnagar,
 555 and Chiba sites, estimated from the CHASER simulated HCHO and NO_2 surface concentrations and VCD. The
 556 simulated data from 07:00 – 18:00 in 2017 were used to estimate the F values. The error bars represent the one
 557 sigma standard deviation of the mean values.
 558

559 The F values for Pantnagar are mostly less than 1, with no distinctive seasonal variation. Mahajan et
560 al. (2015) reported OMI-derived R_{FN} values < 1 over the IGP region. When this estimated conversion
561 factor is used with the values reported by Mahajan et al. (2015), the discrepancy in the satellite and
562 ground-based observation derived R_{FN} values in the IGP region are reduced indicating that the estimated
563 F values for the Pantnagar site can be representative for the IGP region. The F values at the Phimai site
564 range were 0.5–1. Our estimated F values for the Phimai and Pantnagar sites are useful as representative
565 values for these respective regions, which can be improved further based on the results.

566

567 **3.2 Global Evaluation of the CHASER model**

568 This section describes the evaluation of CHASER NO₂ and HCHO columns for 2017 against OMI
569 observations. The OMI AKs were applied to the CHASER outputs to account for the altitude-dependence
570 of the retrievals. First, 2-hourly simulated profiles (NO₂ and HCHO) were sampled closest to the
571 observation time. Secondly, AKs were applied to the sampled profiles and the mean profile was
572 calculated. Thirdly, both the simulations and observations were averaged on a 2.8° bin grid. The month
573 of July and December were discarded from the NO₂ comparison, because few observations (only five
574 days) were available after filtering.

575 **3.2.1 Comparison between CHASER and OMI NO₂**

576 Figure 7 compares the simulated and observed annual mean tropospheric NO₂ columns. The statistics for
577 the comparison are given in Table 5. The model captured the global spatial variation well with a spatial
578 correlation (r) of 0.70. The mean bias error (MBE) and the root mean square error (RMSE) are
579 respectively, 3×10^{14} and 5.4×10^{14} molecules cm⁻². On a global scale, CHASER estimations are
580 negatively biased by 38% compared to OMI. Actually, studies evaluating global NO₂ simulations with
581 satellite observations have reported similar negative biases (Miyazaki et al., 2012, Sekiya et al., 2018).
582 The spatial representativeness between the model and observation is one potential reasons for such
583 negative biases. However, CHASER simulations at 1.1° improved the MBE and RMSE by 5 and 15%,
584 respectively, compared to simulations at 2.8° (Sekiya et al. 2018). Moreover, Sekiya et al (2018) used
585 NO₂ simulations with an updated inventory and compared the results with OMI observations from 2014.
586 Although they reported a better global spatial correlation ($r > 0.90$), the MBE (2.5×10^{14} molecules cm⁻²)

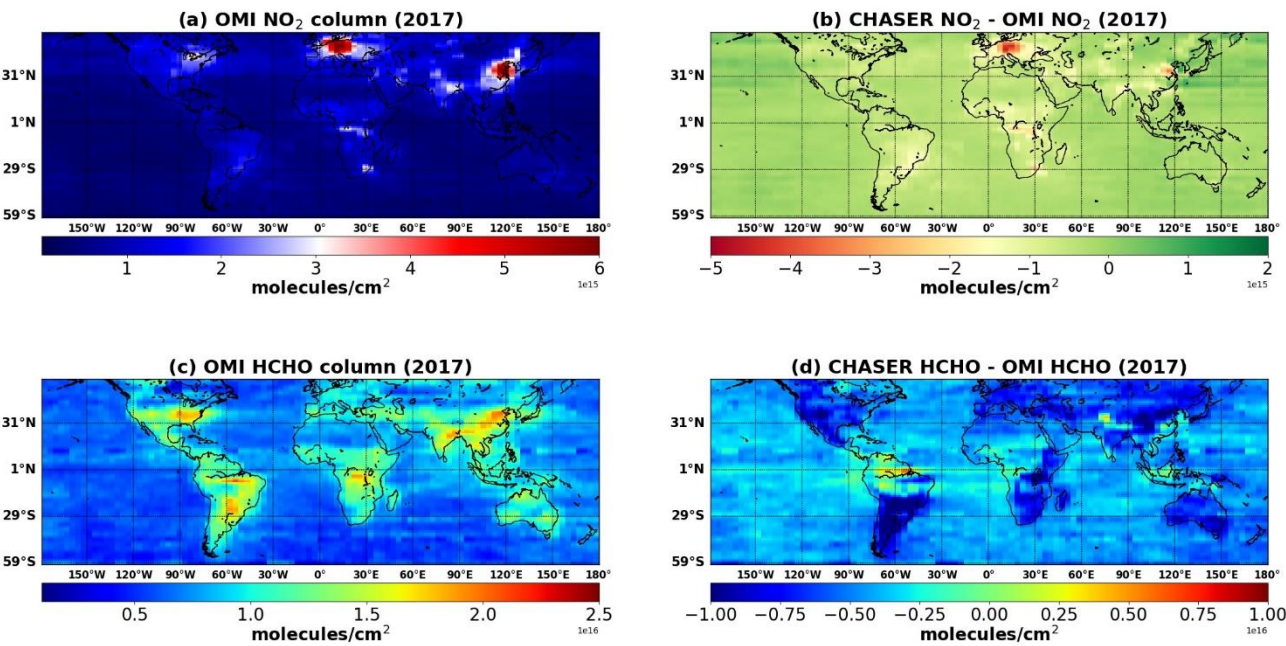
587 and RMSE (4.4×10^{14} molecules cm^{-2}) values at 2.8° resolution are comparable to those obtained from
588 this study.

589 OMI retrievals show the highest NO_2 columns over eastern China (E-China) and Western Europe. Annual
590 mean NO_2 columns over the remainder of the land areas are between 7×10^{14} and 4×10^{15} molecules cm^{-2} .
591 Over the land areas the differences between the datasets are mostly between -2×10^{15} and 5×10^{14} molecules
592 cm^{-2} . Although CHASER also underestimates NO_2 columns over the ocean, although the differences are
593 lower than that of over lands. CHASER estimates are higher by $\sim 5 \times 10^{14}$ molecules cm^{-2} than OMI over
594 Japan. Since 2012, the NO_2 columns have shown a declining trend over Japan, mainly because of emission
595 controls in China (Irie et al 2016). Probably because of simulations with an emission inventory earlier
596 than 2012, the simulated values tend to be higher than observations.

597 Figure 8 compares the seasonal variations in the monthly mean NO_2 columns in some selected region.
598 The error bars represent the 2-sigma standard deviation of the observed mean values. The numbers in
599 each subplot signify the regional spatial correlation between the datasets. Over eastern China (E-China),
600 CHASER values are negatively biased by 24%; the r -value is 0.68. The model captured the seasonality
601 well within variation range of the observations. Over E- and W-USA (eastern and western USA), the
602 respective r -values are 0.85 and 0.49 respectively. Simulated NO_2 columns are higher over E-USA than
603 over W-USA, consistent with the observations. Although, in both regions model estimates are biased by
604 $\sim 23\%$ in the lower side compared to OMI observations, the RMSE in E-USA are $\sim 40\%$ higher than in W-
605 USA.

606 Over Europe, CHASER estimates are negatively biased by 54%, with an r -value and RMSE of 0.80 and
607 1.28×10^{15} molecules cm^{-2} , respectively. The observed NO_2 levels over Europe are almost twice those of
608 the W-USA. The model was unable to capture the regional differences. Model underestimations in Europe
609 can be attributed to the older anthropogenic emission inventory used for the study. In fact, using the HTAP
610 2010 inventory the MBE (-0.53×10^{15} molecules cm^{-2}) between OMI and CHASER NO_2 column

611



613 **Figure 7:** (first column) Annual mean tropospheric (a) NO₂ ($\times 10^{15}$ molecules cm⁻²) and (c) HCHO ($\times 10^{16}$
614 molecules cm⁻²) columns retrieved from OMI observations in 2017. Very limited NO₂ data in July and December
615 met the filtering criteria, thus discarded from the calculation. (second column) The differences between the
616 simulated and observed (c) NO₂ and (d) HCHO columns. All the datasets are mapped onto a 2.8° bin grid.

617

618 simulations at 2.8 over Europe (Sekiya et al. 2018), was $\sim 50\%$ lower than in the current study, although,
619 their RMSE value is similar.

620 Over India, MBE and RMSE for the annual mean NO₂ column are -4.3×10^{14} and 4.4×10^{14} molecules
621 cm⁻², respectively, and the *r*-value is moderate (0.65). Although CHASER estimates are negatively biased
622 by

623

624

625

626 **Table 5:** Statistics of comparison of annual mean NO₂ and HCHO columns between CHASER and OMI.MBE1
 627 and MBE2 are the respective mean bias error. RMSE1 and RMSE2 are the respective root mean square errors. r1
 628 and r2 signifies the respective spatial correlation coefficient. The units of MBE1 and RMSE1 are $\times 10^{15}$ molecules
 629 cm⁻². MBE2 and RMSE2 values are in the unit of $\times 10^{16}$ molecules cm⁻².

Region	r1 (CHASER vs OMI NO ₂)	MBE1 (CHASER - OMI NO ₂)	RMSE1 (CHASER - OMI NO ₂)	r2 (CHASER vs OMI HCHO)	MBE2 (CHASER - OMI HCHO)	RMSE2 (CHASER - OMI HCHO)
Global	0.73	-0.30	0.54	0.74	- 0.45	0.49
E-China	0.68	-1.84	2.47	0.57	-0.63	0.64
E-USA	0.85	-0.62	0.63	0.91	-0.56	0.56
W-USA	0.49	-0.33	0.37	0.63	-0.71	0.71
Europe	0.80	-1.20	1.28	0.51	-0.67	0.68
India	0.65	-0.43	0.44	0.73	-0.56	0.57
N-Africa	0.58	-0.88	0.90	0.65	-0.29	0.32
S-Africa	0.80	-1.25	1.40	0.22	-0.66	0.70
S-America	0.87	-0.80	0.88	0.47	-0.31	0.40
SE Asia	0.57	-0.61	0.64	0.48	-0.41	0.44

630
 631
 632 32%, the values lie within the 2-sigma range of the observations. Sekiya et al. (2018) found no significant
 633 effect of higher model resolution on the MBE and RMSE in the Indian region.
 634 Over N- and S-Africa (North and South Africa), the model values are biased low by more than 75%
 635 compared to the observations. Prominent biomass burning occurs in both regions, which explains the
 636 enhanced NO₂ levels in the OMI retrievals. High negative biases in the model values indicates that
 637 biomass burning NO_x emissions for the African regions are likely underestimated. Similarly, CHASER

underestimates NO₂ columns by 80% in South America, where pyrogenic emissions contributions are significant. CHASER estimates are lower than OMI in these regions, but model captured the spatial distribution well.

Over the SE-Asian (Southeast) region, OMI columns are enhanced during the dry season (i.e., January - April). Burning agricultural wastes is a common practice in many countries in Southeast Asia during the dry season, explaining the enhanced columns. The MBE (-6×10^{14} molecules cm⁻²) and RMSE (6.4×10^{14} molecules cm⁻²) in the SE-Asia region are lower than the African regions (i.e., N-Africa, S-Africa, and S-America), where biomass burning is prominent.

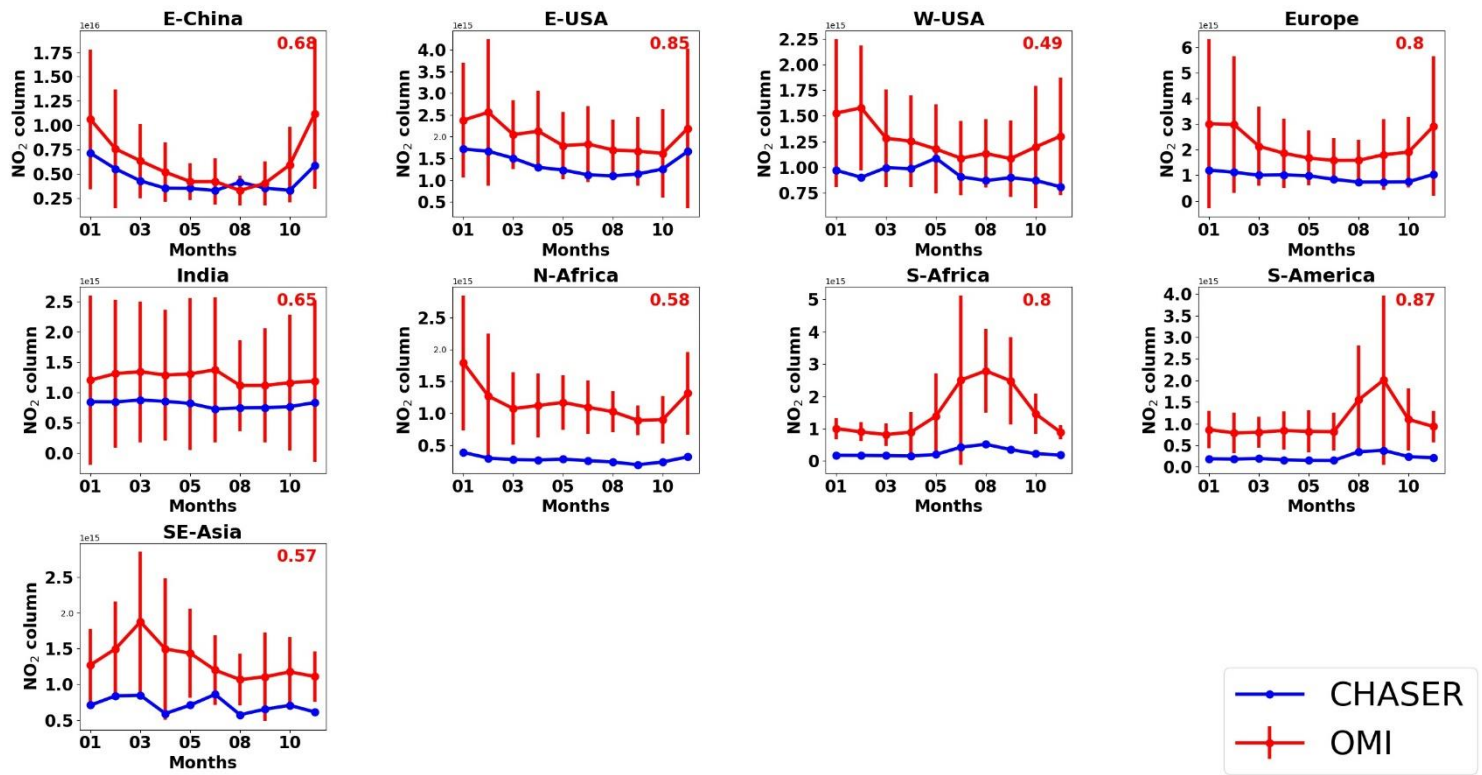


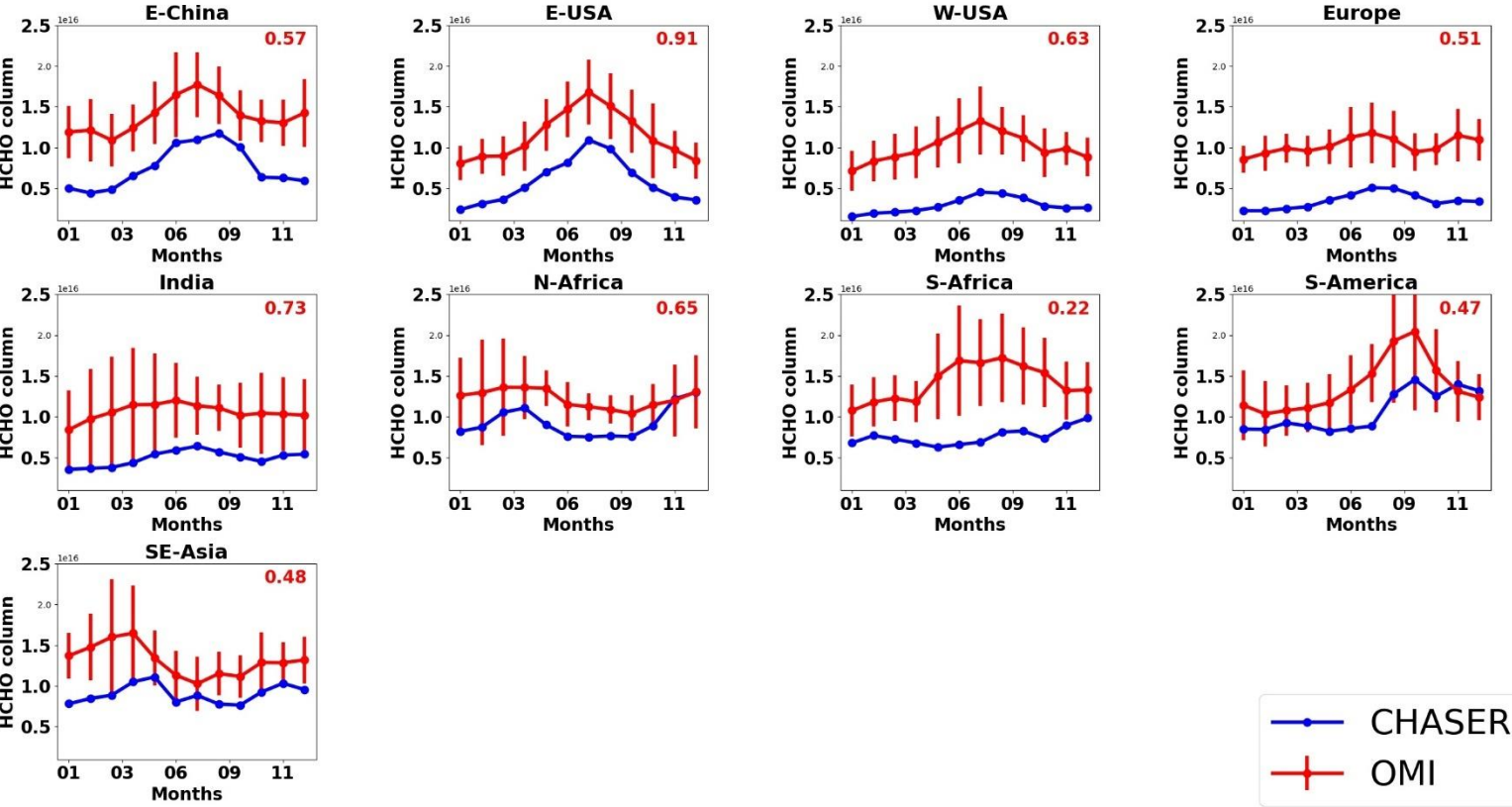
Figure 8: Seasonal variations in tropospheric NO₂ columns in E-China (110° -123° E, 30° - 40° N), E-USA (32° - 43° N, 71° - 95° W), W-USA(32° - 43° N, 100° - 125° W), Europe (35° - 60° N, 0° - 30° E), India (7.5° - 54° N, 68° - 97° E), N-Africa (5° - 15° N, 10° W - 30° E), S-Africa (5° -15° S, 10° -30° E), S-America (0° -20° S, 50° - 70° W), and SE-Asia (10° - 20° N, 9° - 145° E). CHASER simulations and OMI retrievals are plotted in blue and

red colors respectively. The error bars indicate the 2-sigma variation of the observed mean values. The number in the insets signifies the regional spatial correlation between CHASER and OMI NO₂ columns.

3.2.2 Comparison between CHASER and OMI HCHO

Figure 7 presents a comparison between the simulated and observed global annual mean HCHO columns. The statistics of the comparison are given in Table 5. CHASER is able to reproduce the observed global spatial variation well with $r = 0.73$. The global MBE and the RMSE are respectively, -4.5×10^{15} and 4.9×10^{15} molecules cm⁻². MBE and RMSE for monthly mean fields show no distinctive seasonal variation (Table S2). High HCHO columns are observed over China, Australia, Europe, India, Central Africa, South America, and the United States. The model mostly underestimated the HCHO abundances in the higher latitudes and Australia. Absolute differences between the model and observations in the higher latitudes vary between 5×10^{15} and 1×10^{16} molecules cm⁻². Figure 9 compares the seasonal variations in the monthly mean HCHO columns in some selected region. Therein error bars represent the 2-sigma standard deviation of the observed mean values. The numbers in the respective subplots signify the regional spatial correlation between the datasets.

Over E-China, CHASER HCHO estimates are negatively biased by 45% compared to OMI and the r -value is greater than 0.50. The model reproduced the observed HCHO seasonality well including enhanced peaks during the summer. The greatest differences between the datasets are observed during the winter. Over E-USA, the spatial correlation between the datasets is greater than 0.90. Also, the CHASER estimates are biased by 49% in the lower side. Simulations show that the peak in the HCHO abundances occurs in July, which is consistent with the observations. The observed and simulated magnitude of the seasonal modulation is 51 and 78%, respectively. The seasonality in the HCHO columns in E-China and E-USA signifies a strong contribution from biogenic emissions. In both regions, the observed peak HCHO column is $\sim 1.75 \times 10^{16}$ molecules cm⁻². The simulated peak HCHO values are also similar in both regions, despite the underestimation. Over W-USA and Europe, the negative biases in the simulation are greater than 60%. However, the simulated peaks during summer are consistent with the observations. The OMI retrievals show that the HCHO abundances in both regions are almost similar, which has been well captured by CHASER, although the magnitude is underestimated.



681

682 **Figure 9:** Seasonal variations in HCHO columns in E-China (110° -123° E, 30° – 40° N), E-USA (32° – 43° N,
683 71° – 95° W), W-USA(32° – 43° N, 100° – 125° W), Europe (35° – 60° N, 0° – 30° E), India (7.5° – 54° N, 68° –
684 97° E), N-Africa (5° – 15° N, 10° W – 30° E), S-Africa (5° -15° S, 10° -30° E), S-America (0° -20° S, 50° -70° W),
685 and SE-Asia (10° – 20° N, 9° – 145° E). CHASER simulations and OMI retrievals are plotted in blue and red colors
686 respectively. The error bars indicate the 2-sigma variation of the observed mean values. The number in the insets
687 signifies the regional spatial correlation between CHASER and OMI HCHO columns.

688

689 Over India, the model estimates mostly lie outside of the observational variation ranges, although,
690 CHASER captured the spatial distribution well ($r = 0.73$). Magnitudes of the seasonal variation in both
691 OMI and CHASER are around 32%. Between the two African regions, CHASER demonstrated better
692 capability for reproducing HCHO distribution in N-Africa ($r = 0.65$). Negative model bias in N-Africa is

693 almost half (22%) that of S-Africa (46%). Observed N-African HCHO columns are mostly higher than
 694 1.2×10^{16} molecules cm^{-2} during the biomass burning period (November - April). Although the modeled
 695 values are lower than the observed values, the year-end columns (November - December) are similar.
 696 Both datasets show low HCHO variation during May - September. Over the S-African region, the model
 697 capabilities were limited.

698 Over S-America, the negative bias (~22%) in the model estimates compared to the observations is similar
 699 to that of N-Africa. In addition to consistency in the year-end (November to December) columns,
 700 CHASER well reproduced the biomass burning-led enhancements. The observed and simulated
 701 magnitudes of seasonal modulation are 49 and 43%, respectively.

702 Over SE-Asia, CHASER reproduced the observed biomass burning-led enhanced HCHO columns during
 703 the dry season (January - April), however, the occurrence of the peak is inconsistent. As discussed in
 704 section 3.1, observed HCHO peaks related to biomass burning can vary depending on the fire numbers.
 705 The r -value (0.48) is moderate and model is biased by 30% in the lower side. The model negative biases
 706 in the biomass prone regions are lowest (<30%) among the discussed regions.

707 From results of a recent study, De Smedt et al. (2021) reported that, cloud corrections can positively bias
 708 OMI HCHO columns up to 30% compared to Tropospheric Ozone Monitoring Instrument (TROPOMI)
 709 columns. Consequently, uncertainties in the observations are also likely to contribute to the observed
 710 negative biases. Comparison among CHASER, TROPOMI, and OMI HCHO columns is beyond the scope
 711 of this study. However, the effects of uncertainties in the satellite retrievals on the negative biases is
 712 discussed qualitatively and briefly. To demonstrate such effects, CHASER and TROPOMI HCHO
 713 columns for 2019 are compared in Fig S3. The simulation settings and emission inventories are similar
 714 to those explained in section 3.2.3. The comparison results are presented in Table S2. TROPOMI data
 715 has been processed following De Smedt et al. (2021). The CHASER and TROPOMI HCHO spatial
 716 distribution correlates strongly with r -value of 0.78. The values for MBE and RMSE are respectively, -
 717 2.3×10^{15} and 2.8×10^{15} molecules cm^{-2} . Compared to OMI and TROPOMI, CHASER HCHO columns
 718 are negatively biased, respectively, by 61 and 38%. The model biases are lower when compared to
 719 TROPOMI observations. Because of temporal differences in the two comparisons, the biases cannot be

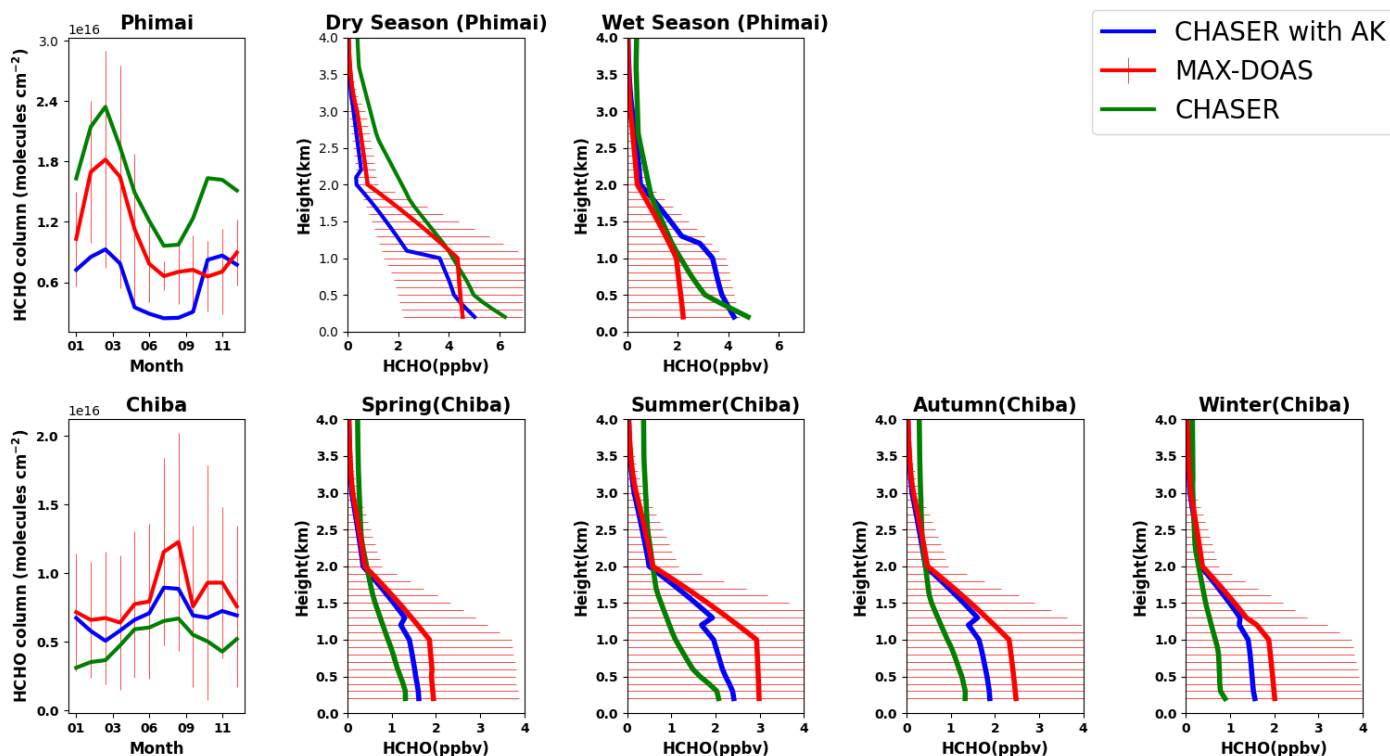
720 compared quantitatively. However, the differences in the biases signify that the observational
721 uncertainties can strongly affect discrepancies between the simulated and observed HCHO abundances.

724 3.3 Evaluation of CHASER simulations at the three sites

725 3.3.1 Evaluation of CHASER HCHO at Phimai and Chiba

726 The seasonally averaged observed and modeled HCHO profiles and partial columns in the 0 - 4 km
727 altitude range at Phimai and Chiba are presented in Fig. 10. The CHASER outputs smoothed with MAX-
728 DOAS averaging kernels (AK) are also depicted. The AK is applied following Franco et al. (2015). First,
729 the CHASER HCHO profiles are interpolated to the MAX-DOAS vertical grids. Next, the MAX-DOAS
730 AK information from individual retrieved profiles is seasonally averaged according to the climate
731 classifications of each site. Finally, the CHASER outputs on the coincident days are selected, and the
732 seasonally averaged AK is applied to the daily mean interpolated profile. Applying individual AKs to the
733 model outputs yielded similar results. The seasonally averaged AKs for both sites are shown in Fig S4.
734 The coincident days at Phimai and Chiba were respectively, 690 and 668.

735 At Phimai, CHASER predicted the increase in the HCHO partial columns during the dry season and
736 well-reproduced the HCHO seasonality. The simulated and observed seasonality correlates strongly with
737 R -value of 0.96. The modeled monthly mean values during the dry season are found to be within the 1σ
738 standard deviation of the observed values, indicating that the pyrogenic emissions estimates used for the
739 simulations are reasonable. CHASER predicted a 41% increase in the HCHO column during January -
740 March, consistent with the observations (41%). CHASER overestimates the HCHO columns in both
741 seasons, and the mean bias error (MBE) (CHASER – MAX-DOAS) is lower (3.7×10^{15} molecules cm^{-2})
742 (Table 6) during the wet season. Although underestimated, the dry season smoothed column values are
743 within the 1σ range.



744 **Figure 10.** Seasonal variations in the HCHO partial columns at 0 - 4 km and vertical profiles during all seasons at
 745 Phimai and Chiba, as inferred from the MAX-DOAS observations (red) and CHASER simulation (green). The
 746 CHASER HCHO partial column and vertical profile smoothed with the MAX-DOAS AK are coloured blue. The
 747 AK information of all the screened (as explained in section 2.2) retrievals were averaged based on the seasonal
 748 classification of the respective sites. The coincident time and date between the model and observations are selected
 749 only. Error bars indicate the one sigma standard deviation of mean values of the MAX-DOAS observations.

750

751 The modeled and observed HCHO mixing ratios in the 1- 2km layers during the wet season are almost
 752 identical, whereas VMR near the surface (i.e., 0 - 1 km) differ by 30%. The absolute mean difference in
 753 the 0-4 km layer is ~0.45ppbv, with the maximum difference of 2.58 ppbv below 200 m. CHASER has
 754 demonstrated good capabilities for reproducing the HCHO profile in the 0.5 – 4 km layer during the wet
 755 season. The significance of AK information is low for the wet season. However, smoothing the model
 756 profiles reduces the overall MBE by 43%.

757

Table 6: Comparison of the seasonal mean HCHO partial columns and profiles (0-4 km) between MAX-DOAS and CHASER at Phimai and Chiba. MBE (CHASER – MAX-DOAS) is the mean bias error. The partial column and profile MBE units are respectively, $\times 10^{16}$ molecules cm^{-2} and ppbv, respectively.

Site	Season	Partial column MBE	Smoothed Partial column MBE	Profile MBE	Smoothed Profile MBE
Phimai	Overall	0.28	-0.07	0.35	0.01
Phimai	Dry	0.37	-0.28	0.58	-0.38
Phimai	Wet	0.21	0.07	0.45	0.33
Chiba	Overall	-0.12	-0.05	-0.37	-0.11
Chiba	Spring	-0.07	-0.04	-0.22	-0.12
Chiba	Summer	-0.16	-0.08	-0.45	-0.26
Chiba	Autumn	-0.10	-0.04	-0.40	-0.19
Chiba	Winter	-0.09	-0.01	-0.42	0.11

During the dry season, the **respective** absolute mean and maximum difference in the datasets in the 0 -1 km layers is ~1 and ~2ppbv. The observed and simulated seasonal differences in the 0-1 km are 50 and 34%, respectively. **Simulated dry season profile values at the heights greater than** ~2 km are out of the 1σ variation range. The two-potential reasons for such differences are lower measurement sensitivity in the free troposphere and **the overestimated Southeast Asian** biogenic emissions in the model. Despite the measurement limitations, CHASER and MAX-DOAS wet season profiles up to 3 km are consistent. Consequently, it is likely that the biogenic emissions **for this region** in the model are overestimated. **The Southeast Asian isoprene emissions in CHASER is 128 Tgyr⁻¹, higher than the CMAS-GLO-BIO (Sindelarova et al., 2022) inventory (78 Tgyr-1). However,** the dry season HCHO profiles in 0 - 2 km are well simulated. **Smoothing** underestimates the dry season profile within the 1σ **variation** range but improved simulations below 200 m. **At heights greater than** 3 km, the smoothed values mostly **reproduce** the a priori **because of** reduced measurement sensitivity (i.e., low AK value, indicating limited information was retrievable).

777 Moderate correlation ($R=0.58$) can be observed between the modeled and observed HCHO partial
778 columns at Chiba. CHASER was able to reproduce the peak in the partial columns in August. The model
779 predicts a 41% increase in the HCHO columns during January - August, whereas the observed increase
780 is 54%. Although Chiba is an urban site, the HCHO and temperature seasonal variations show a tight
781 correlation ($R\sim 0.70$) (Fig S5), suggesting that changes in biogenic emissions modulate HCHO
782 seasonality. Similarly, the modeled seasonality is consistent with temperature variation (Fig. S4). Thus,
783 the simulated HCHO seasonality in Chiba is reasonable, despite underestimation of absolute values.
784 Smoothing the simulations improve the correlation, and the MBE is reduced by 54% (Table 6).

785 The CHASER HCHO profiles in the 0 - 4 km layers are lower than the observations, with an MBE
786 of 0.39 ppbv. The absolute differences in the modeled and retrieved HCHO profiles in the 0-2 km layer
787 during all seasons are higher than at Phimai. Absolute mean differences of ~ 1 ppbv and higher are mainly
788 observed for 0 to 2 km. In addition, the vertical gradients of the simulated profiles are low compared to
789 those at Phimai. The modeled profiles at Chiba resemble the HCHO profiles measured over the ocean
790 during the INTEX-B (Intercontinental Chemical Transport Experiment: Phase B) (Boeke et al., 2011).
791 The Chiba site is near the sea, and coarse CHASER resolution includes the ocean pixels. Moreover, urban
792 surfaces are not homogeneous. Thus, a significant part of the profile discrepancies is likely related to the
793 systematic differences, in addition to emission estimates. However, the model estimates lie within the
794 standard deviation range of the measurements. Because of the low gradients in the simulated profiles, the
795 smoothed profiles mostly imitated the a priori values even below 2 km. Overall, the differences between
796 the observations and smoothed profile are statistically insignificant. Effects of the horizontal resolution
797 on the simulated HCHO levels is discussed in section 3.3.4.

798

799

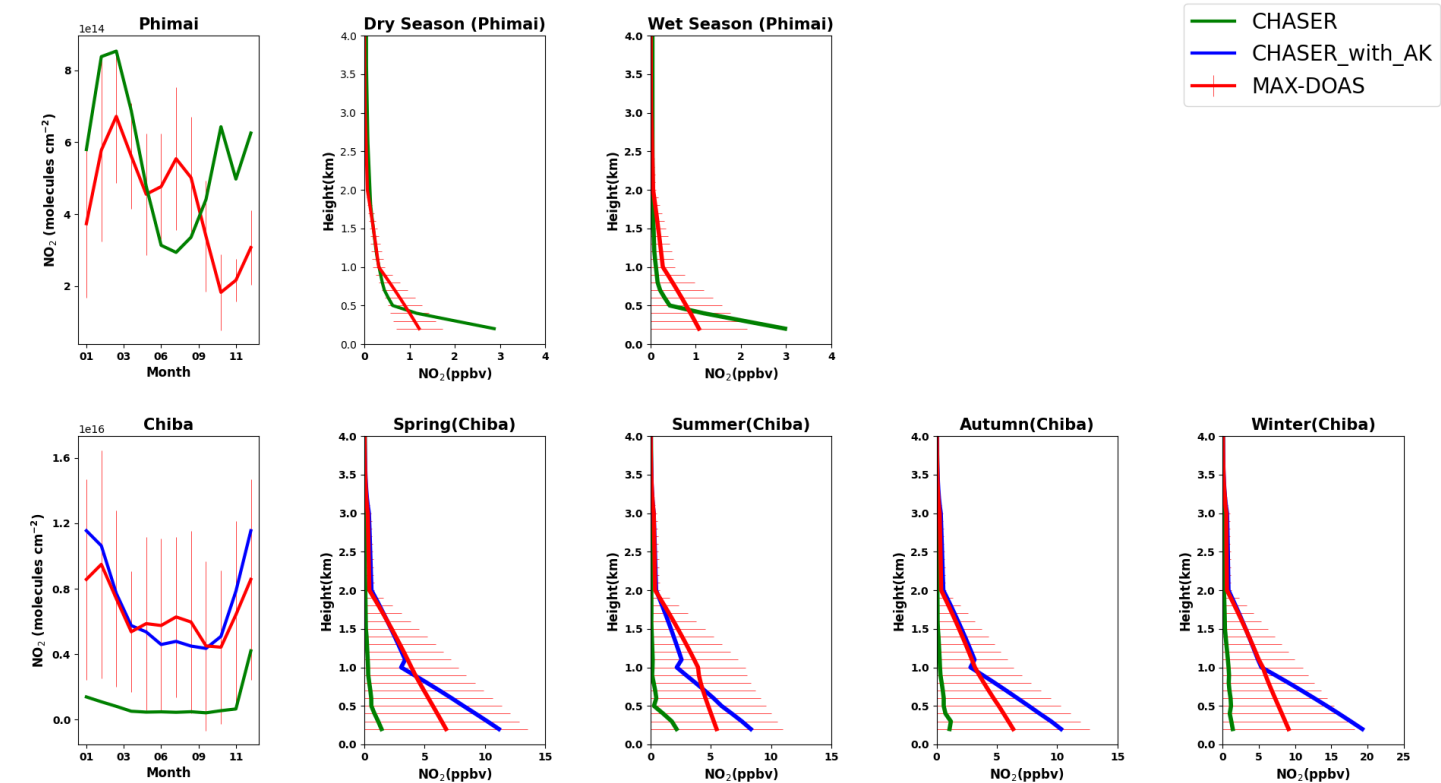
800 3.3.2 Evaluation of CHASER NO₂ in Phimai and Chiba

801 Figure 11 presents the seasonal averages of the MAX-DOAS and CHASER NO₂ profiles and partial
802 columns (0 - 4 km) at Phimai and Chiba. The AK is applied to the modeled outputs for the Chiba site
803 only.

804 Figure S5 of the supplementary information presents a comparison of the observations, model, and
805 smoothed model profiles averaged within the 0 - 2 km layer at Phimai. Smoothing with different a priori
806 values is depicted to demonstrate the effects of the a priori values. The smoothed NO₂ concentrations,
807 calculated using the original a priori values, show a seasonal variation shift. The mean smoothed profile
808 resembles the observations when a priori values are reduced by 50%; however, the dry season values are
809 similar in both cases. Two test cases of smoothing profiles using apriori values above 500 and 800 m
810 shows good agreement with the observations; however, the results are sensitive to the apriori values.
811 Because smoothed profiles are strongly biased to the apriori choice, the smoothing results obtained for
812 the Phimai site are discarded.

813 The modeled NO₂ partial column at Phimai shows good agreement with observations made during the
814 dry season. CHASER well reproduces the enhanced NO₂ columns attributable to biomass burning within
815 the standard deviation of the observations. The peak in the NO₂ levels during March is consistent in both
816 datasets. Although the seasonality does not agree in other months, the overall MBE is 8×10^{13} molecule
817 cm⁻² (Table 7). Above 500 m, the datasets shows excellent agreement. The absolute mean differences in
818 the 0 - 1km layer are 0.22 ppbv, and the maximum difference of ~1.9 ppbv is observed near the surface.
819 Amidst the biomass burning influence, the NO₂ concentrations at Phimai are mostly < 1 ppbv. Thus, the
820 results of comparisons demonstrate CHASER's good capabilities in regions characterized by low NO₂
821 concentrations. Moreover, when NO₂ concentrations are less than < 1 ppbv, the AK information seems
822 less significant if the model can capture low-concentration scenarios.

823



826 **Figure 11.** Seasonal variation in NO_2 partial columns from 0 - 4 km and vertical profiles during all seasons at
827 Phimai and Chiba, as inferred from the MAX-DOAS observations (red) and CHASER simulation (green). The
828 CHASER NO_2 partial column and vertical profile smoothed with the MAX-DOAS AK are coloured in blue. The
829 coincident time and date between the model and observations are selected only. The error bars represent the one
830 sigma standard deviation of mean values of the MAX-DOAS observations.

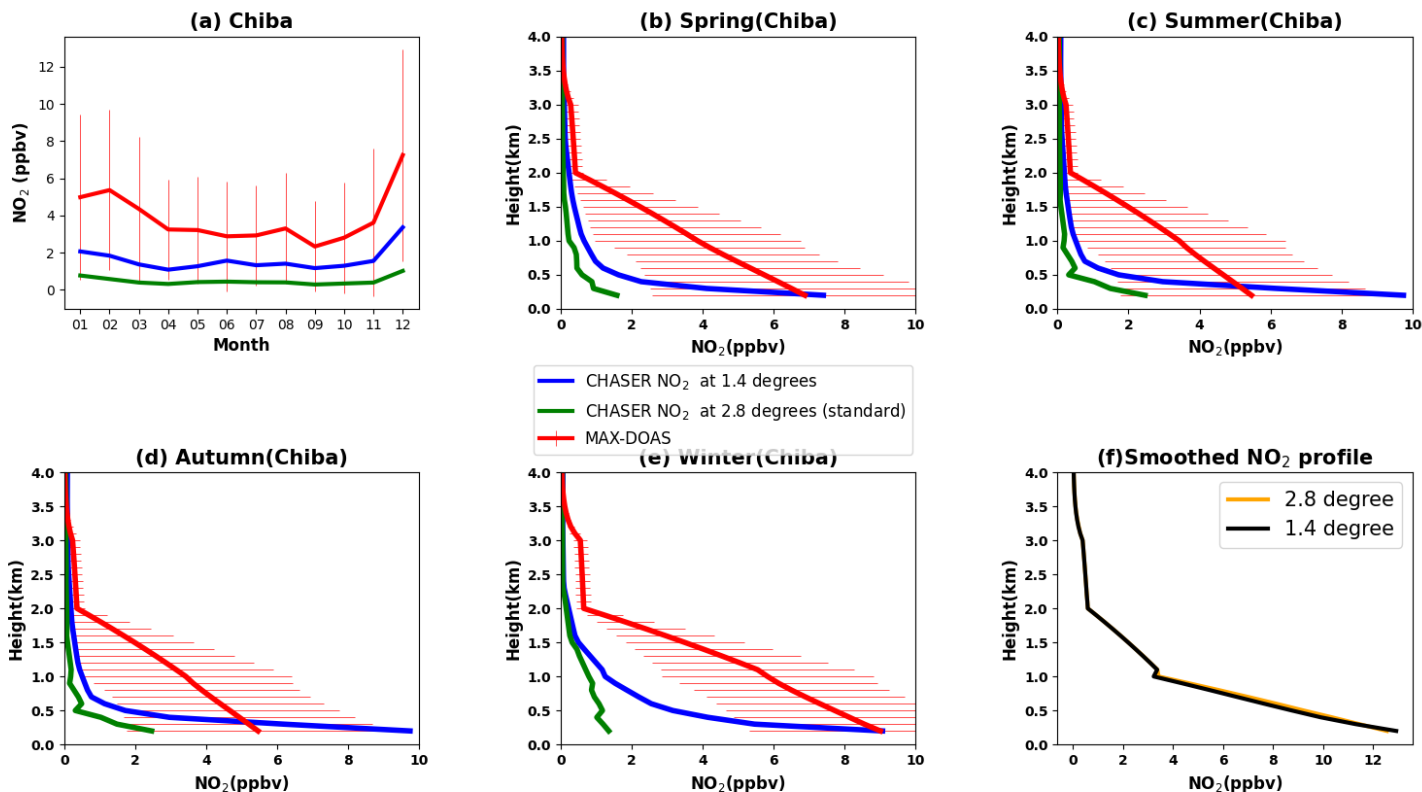
Table 7: Comparison of the seasonal mean NO₂ partial columns and profiles (0-4 km) between MAX-DOAS and CHASER at Phimai and Chiba. MBE (CHASER – MAX-DOAS) is the mean bias error. The partial column and profile MBE units are $\times 10^{15}$ molecules cm⁻² and ppbv, respectively.

Site	Season	Partial column MBE	Smoothed Partial column MBE	Profile MBE	Smoothed Profile MBE
Phimai	Overall	0.08		0.11	
Phimai	Dry	0.18		0.09	
Phimai	Wet	-0.14		0.02	
Chiba	Overall	-5.58	-1.90	-3.27	-1.66
Chiba	Spring	-5.56	-2.00	-3.19	-1.74
Chiba	Summer	-5.52	-2.87	-2.85	-1.86
Chiba	Autumn	-4.57	-1.24	-2.74	-1.40
Chiba	Winter	-6.64	-1.50	-4.30	-1.63

Although the datasets are moderately correlated ($R=0.59$) at Chiba, the model largely underestimates the NO₂ partial column with MBE of $\sim 5 \times 10^{15}$ molecules cm⁻². The model predicts almost constant NO₂ profiles and columns throughout the year. Therefore, the respective seasonal biases are almost similar. The vertical gradient of the modeled NO₂ profiles is also low, too, similarly to the HCHO profiles. The model resolution can be a potential cause for such significant underestimation. The AKs improved the partial column and profiles significantly, reducing the MBE by more than 50%. However, the smoothed profiles and partial columns between the 0 - 2 km layer, differ significantly from the simulations, suggesting that the a priori values strongly affect the smoothed profiles. Consequently, the smoothed NO₂ profiles at Chiba (Fig. S5) are biased to the a priori values, similarly to that of at Phimai (Fig. S5). NO₂ smoothed profile sensitivity to a priori values might be attributable to our retrieval procedure. The a priori data are taken from the measured SCD and retrieved VCD values. As a result, the values are sensitive in the 0 - 2 km layer, similarly to the observations. Using a priori values other than those obtained from observations can affect such sensitivity. The smoothing sensitivity to a priori values is stronger for NO₂ than HCHO. The NO₂ profile gradient is higher than that of HCHO (Figs. 10 and 11), which means that,

854 within 10 km (MAX-DOAS horizontal resolution), the NO₂ mixing ratio and a priori variability (sources
855 and sinks) is higher than those of HCHO, leading to a stronger a priori effect on the smoothed profiles.
856

857 The mean NO₂ mixing ratios in the 0 - 2 km layer in 2018, simulated at spatial resolutions of $2.8^{\circ} \times 2.8^{\circ}$
858 (standard) and $1.4^{\circ} \times 1.4^{\circ}$, are compared with observations at Chiba, as depicted in Fig.12. The error bars
859 are the 1σ standard deviation of the observations. Higher resolution simulations reduced the overall MBE
860 by 35% (Table 8). NO₂ concentrations at 1.4° are now within the variation range of the observations. The
861 1.4° simulation captured the NO₂ seasonal variability better than at 2.8° . Despite improved resolution, the
862 model values are underestimated, with the highest MBE during the winter. According to Miyazaki et al.
863 (2020), the seasonality in the anthropogenic emissions, primarily wintertime heating, is not well
864 represented in the emission inventories, which could likely underestimate winter NO₂ levels. The best
865 agreement between the datasets is observed during summer and spring, with an MBE of ~1 ppbv on a
866 seasonal scale.
867



868 **Figure 12:** (a) Seasonal variations in the NO₂ mixing ratios in the 0 - 2 km layer at Chiba, as inferred from the
 869 MAX-DOAS observations (red) and two CHASER simulations at 2.8°(green) and 1.4°(blue) resolutions. The
 870 simulated NO₂ profiles at 2.8°(green) and 1.4°(blue) resolutions during (b) spring, (c) summer, (d) autumn, and (e)
 871 winter are shown with the observed seasonal profiles at Chiba. Only data (both observed and simulated) for 2018
 872 are plotted. The coincident time and date between the model and observations are selected only. The error bars in
 873 (a), (b), (c), and (d) represent the one sigma standard deviation of mean values of the MAX-DOAS observations.

874

875

876 NO₂ profiles at 2.8° and 1.4° resolution are shown in Figs. 12(b - e). A strong effect of the increased
 877 resolution is observed below 500 m, reducing the negative bias by 70% near the surface. Above 500 m,
 878 the effects of higher resolution are limited, with an MBE reduction of 12% in the 0.6 – 2 km. Although
 879 the near-surface NO₂ concentrations at 1.4° resolution are overestimated, the values are within the
 880 standard deviation of the observations. At around 200m, winter mean NO₂ concentrations at 1.4°

881 resolution are identical to the observations (~9 ppbv), and the summer mean is overestimated. Moreover,
882 the NO₂ levels above 2 km are similar at both resolutions. The resolution effects on NO₂ profiles vary
883 with the location and season (Williams et al., 2017). For example, CHASER NO₂ at 1.1° resolution
884 improved the agreement with aircraft observations below 650 hPa significantly over the Denver
885 metropolitan area (Sekiya et al. 2018), whereas, at Chiba, the 1.4° resolution improved the surface
886 estimates. Consequently, the horizontal resolution is not the only reason for the model underestimation.
887 Other factors such as the vertical resolution, uncertainties in emission inventories, and chemical kinetics,
888 can also affect the simulated NO₂ estimates. Effects of the emission inventory is discussed in section
889 3.3.4.

890 Figure 12(f) shows the smoothed NO₂ profiles at both resolutions. Although the profile shapes are
891 different, the smoothed profiles are almost identical, which demonstrates that, smoothed NO₂ profile
892 sensitivity to a priori choice is mostly independent of the model resolution.

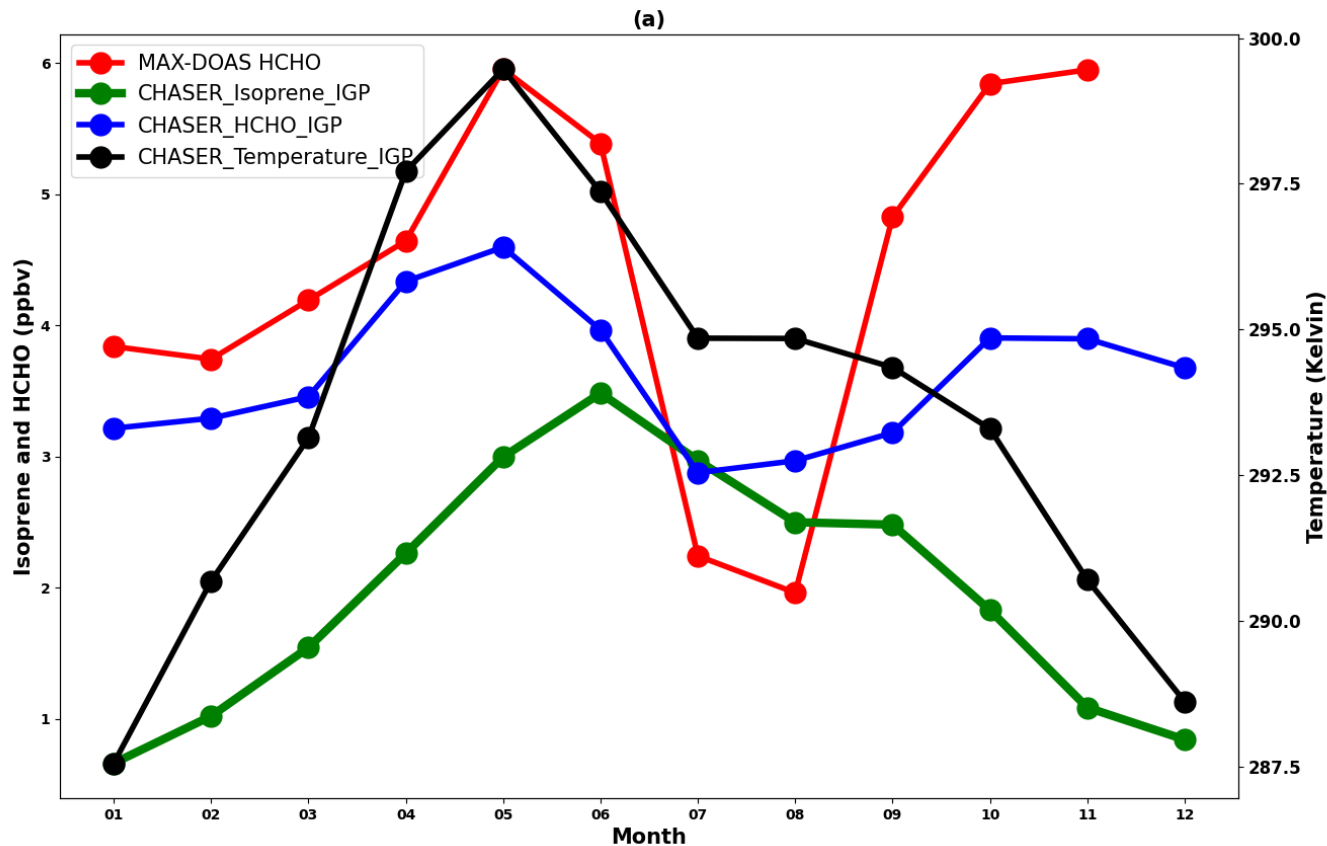
893
894 **Table 8:** Comparison of the seasonal mean NO₂ profiles (0-2 km) among MAX-DOAS and CHASER simulations
895 at 2.8° and 1.4° resolutions at Chiba. MBE at (CHASER – MAX-DOAS) 1.4° and 2.8° are the mean bias error at
896 the respective resolutions. The MBE unit is ppbv.

Season	MBE at 1.4°	MBE at 2.8°
Overall	-2.24	-3.37
Spring	-2.26	-3.23
Summer	-1.50	-2.47
Autumn	-1.57	-2.57
Winter	-3.44	-5.07

897
898
899
900
901

902 **3.3.3 Evaluation of CHASER HCHO in the IGP region**

903 The IGP is the most fertile region in South Asia, which accounts for approximately 50% of the total
904 agricultural production of India and is one of the significant contributing regions to the global greening
905 based on leaf area index (Sarmah et al., 2021). Moreover, IGP is one of the regional HCHO hotspots in
906 India (Chutia et al., 2019). The observed HCHO seasonality at Pantnagar is consistent with that reported
907 by Mahajan et al. (2015) for the entire IGP region. Consequently, comparison with the HCHO retrievals
908 in Pantnagar can assess the model capability in the IGP region. The spatial representiveness is a
909 limitation for comparison between a point measurement and regional simulations. Thus, the results are
910 interpreted qualitatively. Because of the availability of a dataset with continuous observatios, only the
911 comparison for 2017 is shown in Fig. 13.



912

913 **Figure 13.** Seasonal variations in the MAX-DOAS (red) and CHASER (blue) HCHO concentrations at Pantnagar
914 and the IGP region, respectively, in 2017. The coincident dates between the observations and model are plotted

only. The CHASER simulated isoprene and temperature seasonality are shown respectively, in green and black colours. Only the daytime simulated values were considered for the plot.

The modeled HCHO seasonal variations in the IGP region correlate well with the observations at Pantnagar ($R \sim 0.80$). The enhancement in the HCHO concentrations during the spring and post-monsoon season is well reproduced by CHASER, which indicates that CHASER can capture HCHO variation in complex terrain region such as IGP. Figure 13 also depicts the isoprene concentrations and temperature in the IGP region, in addition to the HCHO concentrations. Oxidization of precursor hydrocarbons and photochemical reactions are the most dominant sources of HCHO. Also, isoprene is the most abundant hydrocarbon in the atmosphere. The average ambient isoprene concentrations during July, August, and September in the IGP region are 1.4 ± 0.3 ppbv (Mishra et al., 2020). Therefore, the CHASER isoprene concentration range of $1.5 - 2$ ppbv during the monsoon season seems reasonable. The HCHO concentrations in the IGP region reach a peak during the spring and post-monsoon seasons. A strong correlation between HCHO, isoprene, and temperature variation ($R \sim 0.90$) during the first half of the year indicates that the change in biogenic emissions strongly drives the HCHO seasonal modulation. The observed enhancement in the HCHO levels during spring at Pantnagar is related to biomass burning. The biomass burning events are primarily concentrated in the northwest IGP region (Kumar and Sinha, 2021), where the site is located. On a regional scale, the biomass burning effects is expected to smear. Thus, the strong effect of the biogenic emission on the regional HCHO modulation is reasonable. HCHO modulation differs from isoprene and temperature during the post-monsoon period, suggesting a greater role of biomass burning and anthropogenic emissions. Consequently, the physical processes driving the HCHO seasonality in the IGP region are well reflected in the CHASER simulations.

3.3.4 Effects of the model resolution and emission inventories on results

Effects of the spatial resolution on the evaluation results is assessed by comparing the results of CHASER simulations at 2.8° and 1.4° resolutions with the surface observations, as shown in Fig. 14. Only, the simulated surface HCHO and NO_2 concentrations during 2017 are shown only. The statistics are provided in Table 9. For the Pantnagar site, only the simulations are presented. At Phimai, the HCHO simulations

differ by 3%. The standard simulation shows better agreement with the observations. The higher MBE at 1.4° occurred mostly because of the model overestimation during the wet season. The NO₂ mixing ratios at the two resolution differ by 9%. The MBEs for both trace gases at Phimai are less than 1 ppbv. Thus, the HCHO and NO₂ standard simulations at 2.8° can be regarded as reasonable for regions characterized by low NO₂ levels (<1 ppbv). At Chiba, surface NO₂ and HCHO mixing ratios at 1.4° resolution differ respectively, by 61 and 19%. The NO₂ MBE at 1.4° resolution improved significantly, indicating a strong effect of the model resolution. However, discussion in section 3.2.2 showed limited resolution-based improvement in the overall profile. Results for MBE in the HCHO mixing ratios at 1.4° mostly improved during summer. The wintertime HCHO estimates at both resolutions are similar. In contrast to Chiba and Phimai, differences in the HCHO simulations (30%) at Pantnagar are greater than those of NO₂ (3%). The effect of model resolution varying with location and season was also reported by Sekiya et al. (2018). Compared to the other two sites, differences in the NO₂ simulations at Chiba are larger. This finding is consistent with the results by William et al (2017), which found larger differences with changing model resolution over urban areas.

Although the NO_x estimates for the low NO₂ regions seem reasonable, global NO_x emissions have changed since 2008(i.e., EDGAR-HTAP (2008) emissions used for this study). A recent study by Miyazaki et al. (2020) reported changes in global NO_x emissions from 2005 to 2018. They found a continuous 30% increase in NO_x emissions in India since 2005. REAS v3 (Regional Emission inventory in Asia version 3) inventory estimated a 23% increase in NO_x emissions in India between 2010 - 2015, and power plants were the most significant contributor. Many power plants are clustered along the IGP region (Nair et al., 2007). Thus, the current simulation settings are likely to underestimate the NO₂ mixing ratios and columns in the IGP region. Figure S7 presents comparison of CHASER and OMI NO₂ columns for 2017 over the IGP region. Although the modeled columns are biased by 32% in the lower side, the spatial correlation between the datasets is high ($r=0.78$). CHASER values lie within the range of variation of the observations. Although underestimated, NO₂ estimates in the IGP based on the current inventory are yet reasonable. Sekiya et al., (2018) used higher model resolution and updated emission inventory (HTAP 2010 for simulations in 2014) and reported ~30% lower MBE over India. However, the RMSE values of both studies are comparable.

971 NO_x emissions in Japan have shown continuous decline since the execution of pollution control policies
972 in 1970 (Ohara et al., 2020). Irie et al. (2021) reported a declining trend in NO₂ levels in Chiba since
973 2012, echoing results obtained by Miyazaki et al. (2020) throughout Japan. The bias between CHASER
974 and OMI NO₂ column over Japan is non-significant (Fig. S7 and Table S3). Thus, an updated inventory
975 will not substantially affect the comparison results at the Chiba site. NO_x emissions increased
976 considerably in Southeast Asia. CHASER NO₂ estimates for Thailand based on HTAP 2008 inventory
977 are biased by 45% in the lower side compared to OMI (Fig. S7). However, Phimai being a rural site, the
978 NO_x levels are expected to be low. Changes in biomass burning NO_x estimates are likely to affect the
979 model estimates. Because, the NO₂ levels at Phimai are mostly less than 1 ppbv, the effect of updated
980 inventory on the comparison results is expected to be minimal.

981 CHASER HCHO columns over Japan, the IGP region, and Thailand are negatively biased respectively,
982 by 60, 36, and 32% compared to OMI observations, with *r*-values of 0.5 – 0.7 (Fig. S7). Surl et al. (2018)
983 reported spatial correlation of ~0.5 between GEOS-CHEM and OMI over the IGP region. Anthropogenic
984 VOC emissions in India and other Asian cities have increased since 2005, whereas a negative trend has
985 been observed over Japan (Bauwens et al., 2022). The REAS inventory estimated a 5% increase in
986 NMVOCs in India since 2005. Moreover, anthropogenic emission contributes strongly to the HCHO
987 abundances in the IGP region (Kumar and Sinha 2021). Thus, updated anthropogenic VOC emission
988 inventory is likely to improve the model HCHO estimates in the study regions. However, the formation
989 pathway of HCHO from isoprene emissions is a non-linear function of NO_x chemistry. Consequently, the
990 effects of NO_x emissions changes on the overall HCHO simulations cannot be assessed based on current
991 analyses explained herein.

992

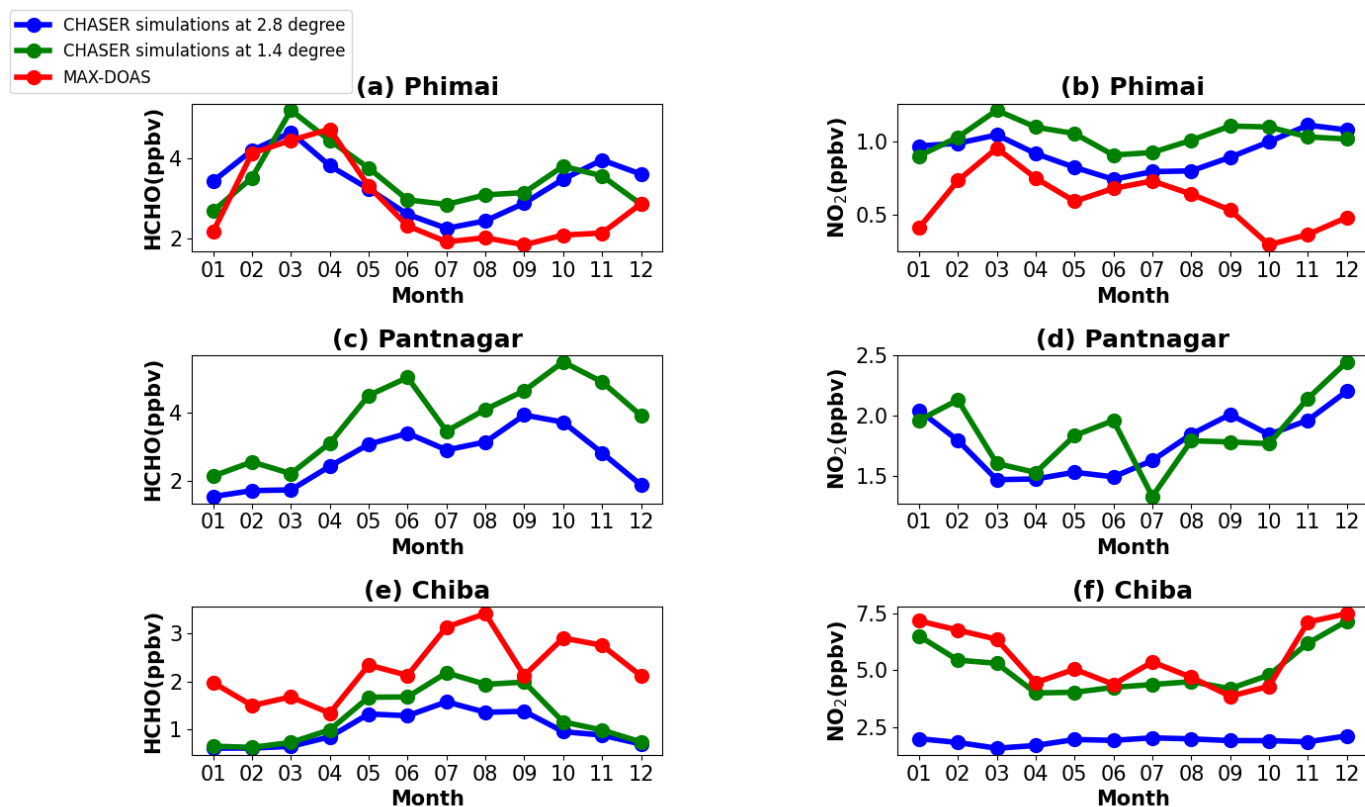


Figure 14. Seasonal variation in the surface HCHO and NO₂ mixing ratios at (a & b) Phimai, (c & d) Pantnagar, and (e & f) Chiba simulated at spatial resolutions of $2.8^{\circ} \times 2.8^{\circ}$ (blue) and $1.4^{\circ} \times 1.4^{\circ}$ (green). Coincident MAX-DOAS NO₂ and HCHO VMRs in the 0-1 km layer at Phimai and Chiba are plotted in red. Observation at Pantnagar are discarded. Only the datasets for 2017 are plotted.

1007
1008
1009
1010
1011

Table 9: The comparison between the observations and simulations at 2.8° and 1.4° spatial resolutions. The MBE is the mean bias error. The unit of MBE is ppbv.

Site	Trace gas	MBE at 2.8°	MBE at 1.4°	Differences between the simulations
Phimai	HCHO	0.54	0.65	3%
Phimai	NO ₂	0.33	0.43	9%
Chiba	HCHO	-1.27	-1.00	19%
Chiba	NO ₂	-0.52	-3.69	61%
Pantnagar				30%
Pantnagar				3%

1012
1013
1014
1015
1016

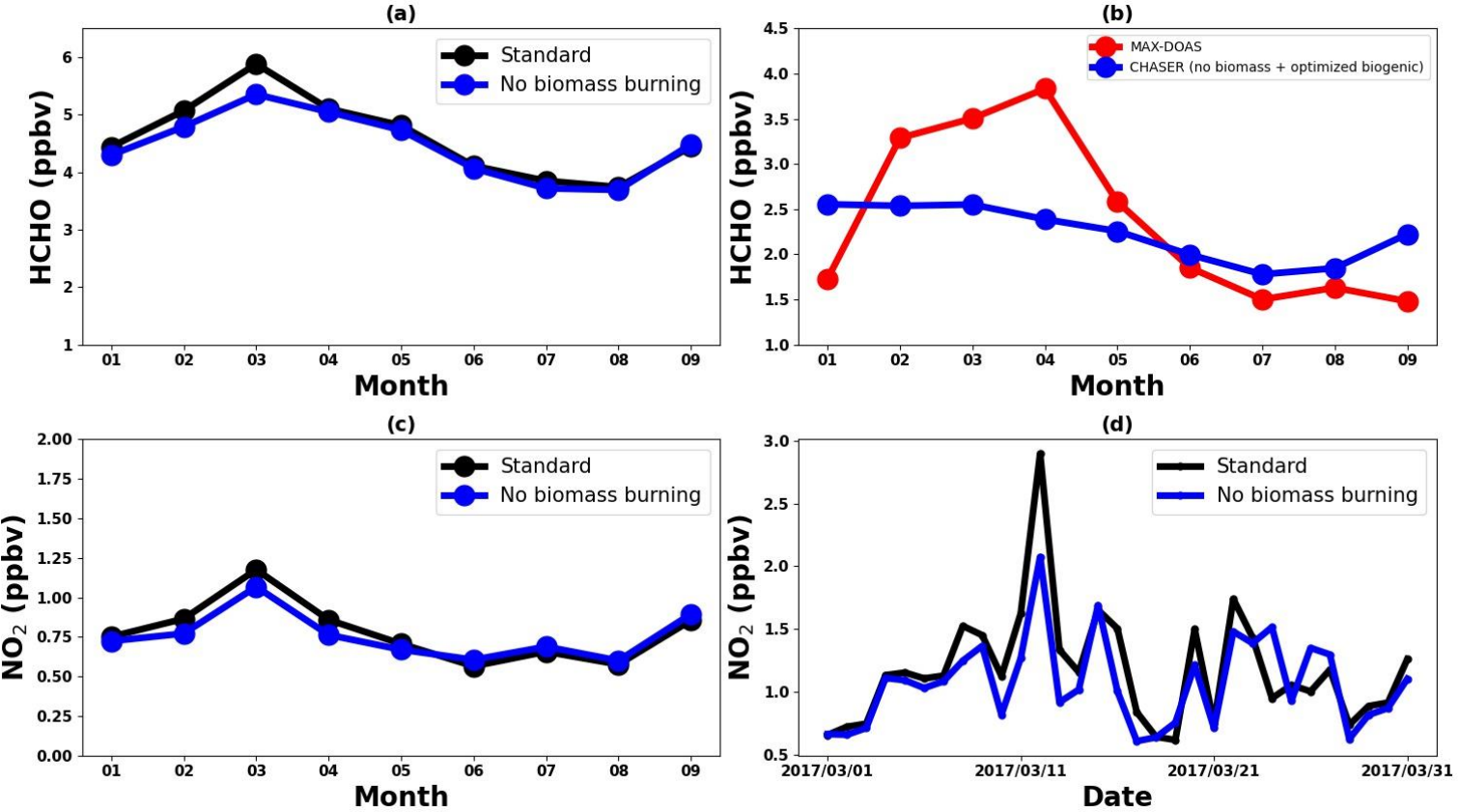
3.4 Contribution estimates

3.4.1 Contribution from biomass burning to the HCHO and NO₂ abundances at Phimai

Good agreement between the datasets in the 0 - 1 km layer at Phimai can quantify biomass burning contributions to the HCHO and NO₂ concentrations. Figure 15 presents results of simulations L1_HCHO, L1_opt, and L1_NO₂. The simulation settings are presented in Table 3. For better readability, the switched-off emissions criterion is described in the legends of Fig. 15. The plots present mean mixing ratios in the 0 – 1 km layer. Biomass burning contributes ~10% to the HCHO concentrations at Phimai during the dry season. However, based on the observations, a greater effect of biomass burning is expected. During the wet season, the MAX-DOAS and CHASER HCHO surface mixing ratios are, respectively, ~2 and ~4 ppbv (Fig. 10), indicating overestimation of the biogenic emissions in CHASER. Figure 15(b) shows the HCHO concentration obtained from simulation L1_opt and MAX-DOAS observations in 2017. In the L1_opt simulation setting, the biomass burning emissions are switched off;

1028 the biogenic emissions are optimized to reproduce results analogous to those obtained from observations
 1029 during the wet season. In the absence of biomass burning, the surface HCHO concentrations at Phimai
 1030 would be ~2 ppbv, indicating a biomass burning contribution of ~20–50% during the dry season. The
 1031 observed interseason difference in the HCHO concentration at Phimai is ~60%. Consequently, the revised
 1032 biomass burning contribution estimate is more reasonable. Pyrogenic emissions contributions to the NO₂
 1033 concentrations at Phimai are ~10% during the dry season (Fig. 15(c)). Because the NO₂ concentrations
 1034 are low at Phimai, the simulation results obtained for March, when the influence of biomass burning is
 1035 highest, are used to derive a better contribution estimate. In the absence of biomass burning, the NO₂
 1036 concentration during March would be about 0.84 ppbv (Fig. 15(d)), indicating a contribution as high as
 1037 35% to the NO₂ concentrations at Phimai.

1038



1039

1040 **Figure 15.** (top panel) (a) Seasonal variations in the HCHO concentrations in the 0 - 1 km layer at Phimai, as
1041 obtained from the standard and L1_HCHO simulations. Pyrogenic emissions of VOCs are switched off in
1042 L1_HCHO. (b) The HCHO seasonal variation in Phimai in 2017, as obtained from the MAX-DOAS observations
1043 (red) and L1_opt simulations. The pyrogenic VOC emissions were switched off, and the biogenic emissions were
1044 reduced by 50% in L1_opt. The coincident dates between the observation and the simulations are shown only.
1045 (bottom panel) (c) Seasonal variations in the NO₂ surface concentrations at Phimai in 2017, as obtained from the
1046 standard and L1_NO₂ simulations. (d) Standard and L1_NO₂ simulation outputs of the daily mean NO₂ surface
1047 concentrations during March 2017. The pyrogenic NO₂ emissions were switched off in the L1_NO₂ simulation.
1048 Only the daytime values from 09:00 – 15:00 LT are used to calculate the seasonal mean.

1049

1050

1051 3.4.2 Contribution of soil NO_x emissions at Phimai

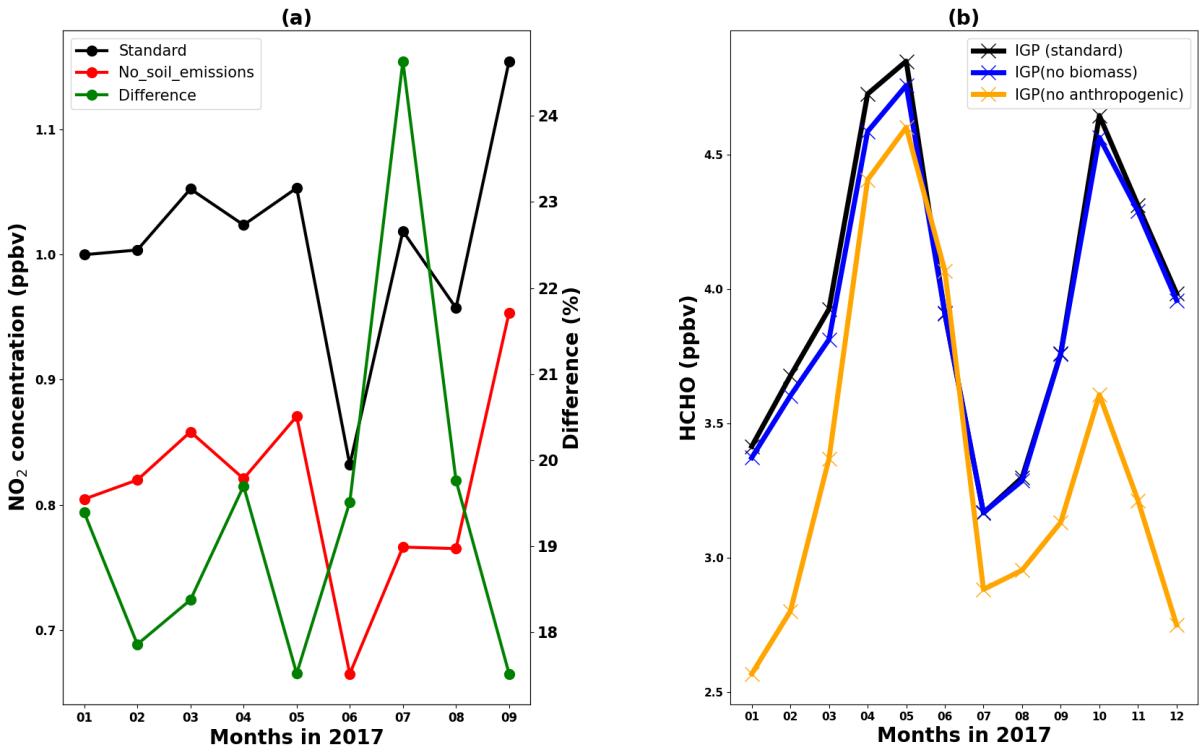
1052 Because soil NO_x emissions are included in CHASER simulations, the NO₂ contributions from soil
1053 emissions are quantified. Figure 16 presents the monthly mean surface NO₂ concentrations at Phimai in
1054 2017, simulated including (standard) and switching off (L1_NO₂) the soil NO_x emissions. The NO₂
1055 concentrations between 09 and 12 hr. were used to calculate the monthly mean concentrations. Soil
1056 emissions contribute ~20% of the overall NO₂ concentrations at Phimai, with higher contributions during
1057 the wet season. The highest soil contribution of about 25% occurs in July.

1058

1059 3.4.3 Contribution from pyrogenic and anthropogenic emissions to the HCHO abundances in the 1060 IGP region

1061 Figure 16(b) presents the standard, L1_HCHO (pyrogenic VOC emissions switched off), and L2
1062 (anthropogenic VOC emissions switched off) HCHO simulations in the IGP region. According to
1063 L1_HCHO simulation results, effects of biomass burning emissions on the regional HCHO modulation
1064 are small (~12%). The HCHO concentrations in India have biogenic, anthropogenic, and pyrogenic VOC
1065 sources. However, biogenic VOCs are the primary driver of the over HCHO variation (Surl et al., 2018).
1066 Consequently, two reasons might be responsible for the small effects of pyrogenic emissions on HCHO
1067 concentrations: (1) Overestimation of the biogenic emission or underestimation of pyrogenic emissions
1068 in the model. (2) Stronger effects of anthropogenic VOC emissions than of pyrogenic VOCs. The L2

1069 simulations show that anthropogenic emissions contribute up to 30% of the HCHO concentration in the
 1070 IGP region, with a maximum contributed during the post-monsoon season, which coincides with the
 1071 lower isoprene concentration (i.e., biogenic emissions) and temperature (Fig. 14). Moreover, Kumar and
 1072 Sinha (2021) reported high acetaldehyde concentrations from anthropogenic emissions in the IGP region
 1073 throughout the year. Consequently, anthropogenic emissions are likely to be a significant driver of HCHO
 1074 concentrations in the IGP region after biogenic emissions.
 1075
 1076



1077
 1078 **Figure 16.** (a) Monthly mean NO₂ concentrations at Phimai were estimated from the standard (black) and L1_NO₂
 1079 (red) simulations. The soil NO_x emissions are switched off in the LI_NO₂ simulation. The green line represents the
 1080 percentage difference between the two simulations. (b) Seasonal variations in the HCHO concentrations in the IGP
 1081 region, obtained from the standard, L1_HCHO (pyrogenic VOC emission switched off), and L2 simulations

1082 (anthropogenic VOC emissions switched off). The simulations for 2017 are shown and analysed. Daytime values
1083 from 09:00-12:00 and 09:00 – 15:00 LT were selected respectively, for Phimai and IGP.
1084

1085 4 Conclusions

1086 Using the JM2 algorithm, NO₂ and HCHO concentrations and profiles were retrieved from MAX-DOAS
1087 observations at three A-SKY sites during January 2017 - December 2018. The retrieved products were
1088 used to evaluate the global chemistry transport model CHASER simulations at the three sites. At all three
1089 locations, the seasonal variation of both trace gases was consistent throughout the investigated period. At
1090 Phimai and Pantnagar, biomass burning led to enhanced HCHO and NO₂ concentrations, respectively,
1091 during the dry season and spring and post-monsoon season. At Chiba, the HCHO variation was consistent
1092 with the temperature-led seasonal changes in biogenic emissions. The changes in the dry season HCHO
1093 and NO₂ levels at Phimai during 2015 - 2018 were consistent with the number of fire events.

1094 The R_{FN} values were biased towards a particular regime when the standard transition range $1 < R_{FN} < 2$
1095 was used. The parameterization of Souri et al. (2020) provides a better estimate of the transition region.
1096 The classification results of the revised transition region at Phimai and Pantnagar contradicted the results
1097 based on the standard transition range. However, they were more reasonable. Such a method based on
1098 observations, is therefore influenced by measurement constraints. More observational evidence must be
1099 accumulated to standardize this method. Overall, the results clarified that the standard transition region is
1100 not valid globally.

1101 Despite the use of an old NO_x emission inventory the simulated NO₂ and HCHO spatial distributions
1102 agreed well with those observed from satellite- observations. The modeled regional NO₂ columns
1103 estimates were within the 2-sigma variability range of OMI NO₂ retrievals. Although the negative bias in
1104 HCHO comparison was higher than that of NO₂, the model demonstrated good capabilities for simulating
1105 the HCHO seasonal variation in different regions.

1106 CHASER showed good capabilities at Phimai, characterized as a VOC-rich and low NO₂ (<1 ppbv)
1107 region. In both seasons, the observed and modeled profiles (HCHO and NO₂) agreed within the one sigma

1108 standard deviation of the measurements, despite general overestimation of the model. Furthermore, both
1109 wet season HCHO profiles were almost identical in the 0.5 – 4 km layer in both datasets.
1110 CHASER demonstrated limited performances at Chiba.NO₂ at higher resolution (i.e.,1.4°) mainly
1111 improved the surface estimates, reducing the overall MBE in the 0 - 2 km layer by 35%. Finer resolution
1112 would improve the HCHO estimates in Chiba by 10%; however, it has yet to be underestimated.
1113 Sensitivity studies for the Phimai site estimated biomass burning contributions to the respective HCHO
1114 and NO₂ concentrations up to ~50 and ~ 35%, respectively. On average, 20% of the NO₂ level originates
1115 from soil NO_x emissions, which increased to 25% in July. Anthropogenic emissions (contribution up to
1116 30%) have a more strongly affect VOC variation in the IGP region than biomass burning, which is
1117 consistent with reports presented in the literature.

1118

1119

1120 *Code availability.* The CHASER and JM2 source codes are not available publicly. Dr. Kengo Sudo
1121 (kengo@nagoya-u.jp) is the contact person for readers and researchers interested in the CHASER model.
1122 In addition, Dr. Hitoshi Irie (hitoshi.irie@chiba-u.jp) will answer queries related to the JM2 codes.

1123

1124 *Data availability:* The MAX-DOAS data used in the study are publicly accessible on the A-SKY network
1125 website (<http://atmos3.cr.chiba-u.jp/a-sky/data.html>). Upon request, the corresponding author can
1126 provide the CHASER simulations and MAX-DOAS averaging kernel data.

1127

1128 *Author contributions:* HMSH conceptualized the study, conducted the model simulations, analysed the
1129 observational and simulation data, and drafted the manuscript. AMF helped with the data processing. HI
1130 developed the JM2 code and maintained the A-SKY network. KS developed the CHASER model and
1131 supervised the study. MN is the PI of the Pantnagar site. AD and MN shared their experience to explain
1132 the results. HI, KS, AD, MN, and AMF commented and provided feedback on the final results and
1133 manuscript.

1134

1135 *Conflict of Interest:* The authors declare that they have no conflict of Interest

1136

1137 *Acknowledgments:* This research is supported by the Global Environmental Research fund (S-12 and S-
1138 20) of the Ministry of the Environment (MOE), Japan, and JSPS KAKENHI Grants: JP20H04320,
1139 JP19H05669, and JP19H04235. The CHASER model simulations are partly performed with the
1140 supercomputer (NEC SX-Aurora TSUBASA) at the National Institute for environmental studies (NIES),
1141 Tsukuba, Japan.

1142

1143

1144 **References**

1145 Amnuaylojaroen, T., Inkom, J., Janta, R., & Surapipith, V. : Long range transport of southeast asian pm2. 5
1146 pollution to northern Thailand during high biomass burning episodes. *Sustainability*, 12(23), 10049. doi:
1147 <https://doi.org/10.3390/su122310049>, 2020
1148

1149 Arlander, D., Brüning, D., Schmidt, U., and Ehhalt, D. : The tropospheric distribution of formaldehyde during
1150 TROPOZ II, *J. Atmos. Chem.*, 22(3), 251-269, <https://doi.org/10.1007/BF00696637>, 1995
1151

1152 Bauwens, M, Verreyken, B, Stavrakou, T, Müller, JF, & De Smedt, I. : Spaceborne evidence for
1153 significant anthropogenic VOC trends in Asian cities over 2005–2019. *Environ. Res. Lett.*, 17(1),
1154 015008. doi:<https://iopscience.iop.org/article/10.1088/1748-9326/ac46eb/>, 2022
1155

1156

1157 Biswas, M. S., Ghude, S. D., Gurnale, D., Prabhakaran, T., and Mahajan, A. S. : Simultaneous Observations of
1158 Nitrogen Dioxide, Formaldehyde and Ozone in the Indo-Gangetic Plain. *Aerosol Air Qual. Res.*, 19(8),
1159 1749-1764, <https://doi.org/10.4209/aaqr.2018.12.0484>, 2019
1160

1161 Biswas, M. S., & Mahajan, A. S. : Year-long Concurrent MAX-DOAS Observations of Nitrogen Dioxide and
1162 Formaldehyde at Pune: Understanding Diurnal and Seasonal Variation Drivers. *Aerosol Air Qual. Res.*,
1163 21(6), 200524. doi:<https://doi.org/10.4209/aaqr.200524> ,2021
1164

1165

1166

1167 Boeke, N. L., Marshall, J. D., Alvarez, S., Chance, K. V., Fried, A., Kurosu, T. P., Rappengluck, B., Richter,
 1168 D.,Walega, J., & Weibring, P. : Formaldehyde columns from the Ozone Monitoring Instrument: Urban
 1169 versus background levels and evaluation using aircraft data and a global model. J.Geophys.Res, 116(D5).
 1170 2011
 1171
 1172
 1173
 1174 Bond, D. W., Zhang, R., Tie, X., Brasseur, G., Huffman, G., Orville, R. E., and Boccippio, D. J. : NO_x production
 1175 by lightning over the continental United States, J. Geophys. Res., 106(D21), 27701-27710,
 1176 <https://doi.org/10.1029/2000JD000191>, 2001
 1177
 1178 Bogumil, K., J. Orphal, T. Homann, S. Voigt, P. Spietz, O. Fleischmann, A. Vogel, M. Hartmann, H. Kromminga,
 1179 and H. Bovensmann : Measurements of molecular absorption spectra with the SCIAMACHY pre-flight
 1180 model: instrument characterization and reference data for atmospheric remote-sensing in the 230–2380 nm
 1181 region, J. Photocho. Photobio. A, 157(2), 167-184, doi:10.1016/S1010-6030(03)00062-5, 2003
 1182
 1183
 1184
 1185
 1186
 1187 Burkert, J., Andrés-Hernández, M. D., Stöbener, D., Burrows, J. P., Weissenmayer, M., & Kraus, A. (2001) :
 1188 Peroxy radical and related trace gas measurements in the boundary layer above the Atlantic Ocean, J.
 1189 Geophys. Res., 106(D6), 5457-5477, <https://doi.org/10.1029/2000JD900613>, 2001
 1190
 1191
 1192
 1193 Cárdenas, L., Rondón, A., Johansson, C., & Sanhueza, E. : Effects of soil moisture, temperature, and inorganic
 1194 nitrogen on nitric oxide emissions from acidic tropical savannah soils. J. Geophys. Res., 98(D8), 14783-
 1195 14790, <https://doi.org/10.1029/93JD01020>, 1993
 1196

1197 Chaliyakunnel, S., Millet, D. B., and Chen, X. : Constraining emissions of volatile organic compounds over the
 1198 Indian subcontinent using space-based formaldehyde measurements. *J. Geophys. Res.*, 124(19), 10525-
 1199 10545, <https://doi.org/10.1029/2019JD031262>, 2019
 1200
 1201
 1202 Chance, K. V., and R. J. D. Spurr. : Ring effect studies: Rayleigh scattering, including molecular
 1203 parameters for rotational Raman scattering: and the Fraunhofer spectrum, *Appl. Opt.* , 36(21),
 1204 5224-5230 doi:10.1364/AO.36.005224,1997
 1205
 1206 Chutia, L., Ojha, N., Girach, I. A., Sahu, L. K., Alvarado, L. M. A., Burrows, J. P., Pathak., P., & Bhuyan, P. K. :
 1207 Distribution of volatile organic compounds over Indian subcontinent during winter: WRF-chem simulation
 1208 versus observations. *Environ. Pollut.*, 252, 256-269. doi:<https://doi.org/10.1016/j.envpol.2019.05.097>,
 1209 2019
 1210
 1211
 1212
 1213 Clémer, K., Van Roozendaal, M., Fayt, C., Hendrick, F., Hermans, C., Pinardi, G., Spurr, R., Wang, P., and De
 1214 Mazière, M. : Multiple wavelength retrieval of tropospheric aerosol optical properties from MAXDOAS
 1215 measurements in Beijing, *Atmos. Meas. Tech.*, 3(4), 863-878, <https://doi.org/10.5194/amt-3-863-2010>,
 1216 2010
 1217
 1218
 1219 Colella, P., & Woodward, P. R. : The piecewise parabolic method (PPM) for gas-dynamical simulations. *J. Comput.*
 1220 *Phys.*, 54(1), 174-201, [https://doi.org/10.1016/0021-9991\(84\)90143-8](https://doi.org/10.1016/0021-9991(84)90143-8), 1984
 1221
 1222
 1223
 1224
 1225 Crutzen, P. J. : The influence of nitrogen oxides on the atmospheric ozone content. *Q. J. Roy. Meteor. Soc.*, 96(408),
 1226 320-325, <https://doi.org/10.1002/qj.49709640815>, 1970
 1227
 1228

Davidson, E. A., Vitousek, P. M., Matson, P. A., Riley, R., García-Méndez, G., & Maass, J. M. : Soil emissions of
nitric oxide in a seasonally dry tropical forest of Mexico. *J. Geophys. Res.*, 96(D8), 15439-15445,
<https://doi.org/10.1029/91JD01476>, 1991

De Smedt, I. , Pinardi, G., Vigouroux, C., Compernelle, S., Bais, A., Benavent, N., Eichmann, K-U., Hedelt, P.,
Hendricks, F., Irie, H., Kumar, V., Lambert, J-C., Langerock, B., Lerot, C., Liu, C., Loyola, D., Pitters, A.,
Riccjter, A., Cardens, C.R., Romahn, F., Ryan, R.G., Sinha, V., Theys, N., Vlietinck, J., Waggoner, T., Wang,
T., YU, H., and Van Roozendael, M.,: Comparative assessment of TROPOMI and OMI formaldehyde
observations and validation against MAX-DOAS network column measurements. *Atmos. Chem. Phys.*,
21(16), 12561-12593. doi:<https://doi.org/10.5194/acp-21-12561-2021>, 2021

Duncan, B. N., Yoshida, Y., Damon, M. R., Douglass, A. R., and Witte, J. C. : Temperature dependence of factors
controlling isoprene emissions. *Geophys. Res. Lett.*, 36(5), <https://doi.org/10.1029/2008GL037090>, 2009

Emori, S., Nozawa, T., Numaguti, A., & Uno, I. : Importance of cumulus parameterization for precipitation
simulation over East Asia in June. *J. Meteorol. Soc. Jpn.*, 79(4), 939-947.
<https://doi.org/10.2151/jmsj.79.939>, 2001

Fleischmann, O. C., M. Hartmann, J. P. Burrows, and J. Orphal : New ultraviolet absorption cross-sections of BrO
at atmospheric temperatures measured by time-windowing Fourier transform spectroscopy, *J. Photocho.*
Photobio. A, 168(1), 117-132, doi:10.1016/j.jphotochem.2004.03.026, 2004

1262 Franco, B., Hendrick, F., Van Roozendaal, M., Müller, J.-F., Stavrakou, T., Marais, E. A., Bovy, B., Bader, W.,
 1263 Fayt, C., Hermans, C., Lejuene, B., Pinardi, G., Sevais, C., and Mahieu, E. : Retrievals of formaldehyde
 1264 from ground-based FTIR and MAX-DOAS observations at the Jungfraujoch station and comparisons with
 1265 GEOS-Chem and IMAGES model simulations. *Atmos. Meas. Tech.*, 8(4), 1733-1756,
 1266 <https://doi.org/10.5194/amt-8-1733-2015>, 2015
 1267
 1268 Fu, T. M., Jacob, D. J., Wittrock, F., Burrows, J. P., Vrekoussis, M., and Henze, D. K. : Global budgets of
 1269 atmospheric glyoxal and methylglyoxal, and implications for formation of secondary organic aerosols, *J.*
 1270 *Geophys. Res.*, 113(D15), <https://doi.org/10.1029/2007JD009505>, 2008
 1271
 1272
 1273 Frieß, U., Monks, P. S., Remedios, J. J., Rozanov, A., Sinreich, R., Wagner, T., & Platt, U. : MAX-DOAS O4
 1274 measurements: A new technique to derive information on atmospheric aerosols: 2. Modeling studies. *J.*
 1275 *Geophys. Res.*, 111(D14), <https://doi.org/10.1029/2005JD006618>, 2006
 1276
 1277 Frieß, U., Klein Baltink, H., Beirle, S., Clémer, K., Hendrick, F., Henzing, B., Irie, H., de Leeuw, G., Li, A.,
 1278 Moerman, M. M., van Roozendaal, M., Shaiganfar, R., Wagner, T., Wang, Y., Xie, P., Yilmaz, S., and
 1279 Zieger, P. : Intercomparison of aerosol extinction profiles retrieved from MAX-DOAS measurements.
 1280 *Atmos. Meas. Tech.*, 9(7), 3205-3222, <https://doi.org/10.5194/amt-9-3205-2016>, 2016
 1281
 1282 Fukushima, A., Kanamori, H., & Matsumoto, J. : Regionality of long-term trends and interannual variation of
 1283 seasonal precipitation over India. *Prog Earth Planet Sci*, 6(1), 1-20. doi:[https://doi.org/10.1186/s40645-](https://doi.org/10.1186/s40645-019-0255-4)
 1284 [019-0255-4](https://doi.org/10.1186/s40645-019-0255-4), 2019
 1285
 1286
 1287 Hak, C., Pundt, I., Trick, S., Kern, C., Platt, U., Dommen, J., Ordóñez, C., Prévôt, A. S. H., Junkermann, W.,
 1288 Astorga-Lloréns, C., Larsen, B. R., Mellqvist, J., Strandberg, A., Yu, Y., Galle, B., Kleffmann, J., Lörzer,
 1289 J. C., Braathen, G. O., and Volkamer, R. : Intercomparison of four different in-situ techniques for ambient
 1290 formaldehyde measurements in urban air, *Atmos. Chem. Phys.*, 5(11), 2881-2900.
 1291 <https://doi.org/10.5194/acp-5-2881-2005>, 2005
 1292
 1293

1294

1295 Hall, S. J., Matson, P. A., and Roth, P. M. : NO_x emissions from soil: implications for air quality modeling in
1296 agricultural regions. *Annu. Rev. Energy Environ.*, 21(1), 311-346.
1297 <https://doi.org/10.1146/annurev.energy.21.1.311>, 1996

1298

1299

1300 Halla, J. D., Wagner, T., Beirle, S., Brook, J. R., Hayden, K. L., O'Brien, J. M., Ng, A., Majonis, D., Wenig, M.
1301 O., and McLaren, R : Determination of tropospheric vertical columns of NO₂ and aerosol optical
1302 properties in a rural setting using MAX-DOAS. *Atmos. Chem. Phys.*, 11(23), 12475-12498,
1303 <https://doi.org/10.5194/acp-11-12475-2011>, 2011

1304

1305

1306 Hendrick, F., Müller, J.-F., Clémer, K., Wang, P., De Mazière, M., Fayt, C., Gielen, C., Hermans, C., Ma, J. Z.,
1307 Pinardi, G., Stavrakou, T., Vlemmix, T., and Van Roozendaal, M.: Four years of ground-based MAX-
1308 DOAS observations of HONO and NO₂ in the Beijing area, *Atmos. Chem. Phys.*, 14(2), 765-781,
1309 <https://doi.org/10.5194/acp-14-765-2014>, 2014

1310

1311

1312 Hermans, C., A. Vandaele, S. Fally, M. Carleer, R. Colin, B. Coquart, A. Jenouvrier, and M.-F. Merienne.
1313 : Absorption cross-section of the collision-induced bands of oxygen from the UV to the NIR, in *Weakly*
1314 *interacting molecular pairs: unconventional absorbers of radiation in the atmosphere*, edited, pp. 193-
1315 202, Springer, 2003.

1316

1317

1318

1319 Hönninger, G., Friedeburg, C. v., and Platt, U. : Multi axis differential optical absorption spectroscopy (MAX-
1320 DOAS), *Atmos. Chem. Phys.*, 4(1), 231-254, <https://doi.org/10.5194/acp-4-231-2004>, 2004

1321

1322 Hoque, H.M. S., Irie, H., and Damiani, A. (2018). First MAX-DOAS Observations of Formaldehyde and Glyoxal
1323 in Phimai, Thailand. *J. Geophys. Res.*, 123(17), 9957-9975, <https://doi.org/10.1029/2018JD028480>, 2018a

1324

1325 Hoque, H. M. S., Irie, H., Damiani, A., Rawat, P., and Naja, M. : First simultaneous observations of formaldehyde
1326 and glyoxal by MAX-DOAS in the Indo-Gangetic Plain region. *Sola.* , [https://doi.org/10.2151/sola.2018-](https://doi.org/10.2151/sola.2018-028)
1327 028, 2018b

1328

1329

1330 Houweling, S., Dentener, F., and Lelieveld, J. : The impact of nonmethane hydrocarbon compounds on tropospheric
1331 photochemistry. *J. Geophys. Res.*, 103(D9), 10673-10696, <https://doi.org/10.1029/97JD03582>, 1998

1332

1333

1334

1335 Huber, D. E., Steiner, A. L., & Kort, E. A. : Daily Cropland Soil NO_x Emissions Identified by TROPOMI and
1336 SMAP. *Geophys. Res. Lett.*, 47(22), e2020GL089949, <https://doi.org/10.1029/2020GL089949>, 2020

1337

1338

1339

1340 Irie, H., Kanaya, Y., Akimoto, H., Iwabuchi, H., Shimizu, A., & Aoki, K. : First retrieval of tropospheric aerosol
1341 profiles using MAX-DOAS and comparison with lidar and sky radiometer measurements. *Atmos. Chem.*
1342 *Phys.*, 8(2), 341-350, <https://doi.org/10.5194/acp-8-341-2008>, 2008a

1343 Irie, H., Kanaya, Y., Akimoto, H., Tanimoto, H., Wang, Z., Gleason, J. F., & Bucsela, E. J. : Validation of OMI
1344 tropospheric NO₂ column data using MAX-DOAS measurements deep inside the North China Plain in
1345 June 2006: Mount Tai Experiment 2006. *Atmos. Chem. Phys.*, 8(22), 6577-
1346 6586,<https://doi.org/10.5194/acp-8-6577-2008>, 2008b.

1347

1348 Irie, H., Kanaya, Y., Akimoto, H., Iwabuchi, H., Shimizu, A., & Aoki, K. : Dual-wavelength aerosol vertical profile
1349 measurements by MAX-DOAS at Tsukuba, Japan. *Atmos. Chem. Phys.*, 9(8), 2741-2749,
1350 <https://doi.org/10.5194/acp-9-2741-2009>, 2009

1351

1352 Irie, H., Takashima, H., Kanaya, Y., Boersma, K., Gast, L., Wittrock, F., Brunner, D., Zhou, Y., Roozendael, M.
1353 V. : Eight-component retrievals from ground-based MAX-DOAS observations. *Atmos. Meas. Tech.*, 4(6),
1354 1027-1044, <https://doi.org/10.5194/amt-4-1027-2011>, 2011

1355

1356 Irie, H., Nakayama, T., Shimizu, A., Yamazaki, A., Nagai, T., Uchiyama, A., Zaizen, Y., Kagamitani, S.,
1357 and Matsumi, Y. : Evaluation of MAX-DOAS aerosol retrievals by coincident observations using CRDS,
1358 lidar, and sky radiometer in Tsukuba, Japan. *Atmos. Meas. Tech.*, 8(7), 2775-2788,
1359 <https://doi.org/10.5194/amt-8-2775-2015>, 2015

1360

1361 Irie, H., Muto, T., Itahashi, S., Kurokawa, J., & Uno, I. : Turnaround of tropospheric nitrogen dioxide pollution
1362 trends in China, Japan, and South Korea. *Sola*, 12, 170-174. doi: <https://doi.org/10.2151/sola.2016-035>,
1363 2016

1364

1365

1366 Irie, H., Yonekawa, D., Damiani, A., Hoque, H.M.S, Sudo, K., & Itahashi, S.; Continuous multi-component MAX-
1367 DOAS observations for the planetary boundary layer ozone variation analysis at Chiba and Tsukuba, Japan,
1368 from 2013 to 2019. *Prog Earth Planet Sci*, 8(1), 1-11. doi:[https://doi.org/10.1186/s40645-021-00424-](https://doi.org/10.1186/s40645-021-00424-9)
1369 9,2021

1370

1371

1372 Ito, A., and Inatomi, M. : Use of a process-based model for assessing the methane budgets of global terrestrial
1373 ecosystems and evaluation of uncertainty. *Biogeosciences*, 9(2), 759-773. [https://doi.org/10.5194/bg-9-](https://doi.org/10.5194/bg-9-759-2012)
1374 759-2012, 2012

1375

1376

1377 Iwabuchi, H. :Efficient Monte Carlo methods for radiative transfer modeling. *J. Atmos. Sci.*, 63(9), 2324-2339,
1378 <https://doi.org/10.1175/JAS3755.1>, 2006

1379

1380

1381 Jang, M., and Kamens, R. M. : Characterization of secondary aerosol from the photooxidation of toluene in the
1382 presence of NO_x and 1-propene, *Environ. Sci. Technol.*, 35(18), 3626-3639.
1383 <https://doi.org/10.1021/es010676+>, 2001

1384

1385

1386 Jin, X., Fiore, A. M., Murray, L. T., Valin, L. C., Lamsal, L. N., Duncan, B., Boersma, K.F., De Smedt, I., Abad,
1387 G.G., Chance, K., and Tonnesen, G. : Evaluating a space-based indicator of surface ozone-NO_x-VOC

sensitivity over midlatitude source regions and application to decadal trends. *J. Geophys. Res.*, 122(19), 10,439-410,461, <https://doi.org/10.1002/2017JD026720>, 2017

Jin, X., & Holloway, T. (2015). Spatial and temporal variability of ozone sensitivity over China observed from the Ozone Monitoring Instrument. *J. Geophys. Res.*, 120(14), 7229-7246. doi: <https://doi.org/10.1002/2015JD023250>

Jenkin, M.E., Young, J.C., & Rickard, A.R. : The MCM v3. 3.1 degradation scheme for isoprene. *Atmos. Chem. Phys.*, 15(20), 11433-11459. doi:<https://doi.org/10.5194/acp-15-11433-2015>, 2015

K-1 model developers : K-1 Coupled GCM (MIROC) description, Tech .rep., Center for Climate System Research (University of Tokyo), National Institute for Environmental Studies, and Frontier Research Center for Global Change, available at : http://ccsr.aori.u-tokyo.ac.jp/~hasumi/miroc_description.pdf, 2004

Kanakidou, M., Seinfeld, J. H., Pandis, S. N., Barnes, I., Dentener, F. J., Facchini, M. C., Van Dingenen, R., Ervens, B., Nenes, A., Nielsen, C. J., Swietlicki, E., Putaud, J. P., Balkanski, Y., Fuzzi, S., Horth, J., Moortgat, G. K., Winterhalter, R., Myhre, C. E. L., Tsigaridis, K., Vignati, E., Stephanou, E. G., and Wilson, J. : Organic aerosol and global climate modelling: a review. *Atmos. Chem. Phys.*, 5(4), 1053-1123, <https://doi.org/10.5194/acp-5-1053-2005>

Kanaya, Y., Irie, H., Takashima, H., Iwabuchi, H., Akimoto, H., Sudo, K., Gu, M., Chong, J., Kim, Y. J., Lee, H., Li, A., Si, F., Xu, J., Xie, P.-H., Liu, W.-Q., Dzhola, A., Postlyakov, O., Ivanov, V., Grechko, E., Terpugova, S., and Panchenko, M.: Long-term MAX-DOAS network observations of NO₂ in Russia and Asia (MADRAS) during the period 2007–2012: instrumentation, elucidation of climatology, and comparisons with OMI satellite observations and global model simulations. *Atmos. Chem. Phys.*, 14(15), 7909-7927, <https://doi.org/10.5194/acp-14-7909-2014>, 2014

- 1421 Kannari, A., Tonooka, Y., Baba, T., & Murano, K. : Development of multiple-species 1km× 1km resolution hourly
 1422 basis emissions inventory for Japan. *Atmos. Environ.*, 41(16), 3428-3439.
 1423 doi:<https://doi.org/10.1016/j.atmosenv.2006.12.015>, 2007
 1424
 1425
- 1426 Khodmanee, S., & Amnuaylojaroen, T., Impact of Biomass Burning on Ozone, Carbon Monoxide, and Nitrogen
 1427 Dioxide in Northern Thailand. *Front. Environ. Sci.*, 9, 27. doi:<https://doi.org/10.3389/fenvs.2021.641877>,
 1428 2021
 1429
- 1430
- 1431 Kreher, K., Van Roozendaal, M., Hendrick, F., Apituley, A., Dimitropoulou, E., Frieß, U., Richter, A., Wagner,
 1432 T., Lampel, J., Abuhassan, N., Ang, L., Anguas, M., Bais, A., Benavent, N., Bösch, T., Bognar, K.,
 1433 Borovski, A., Bruchkouski, I., Cede, A., Chan, K. L., Donner, S., Drosoglou, T., Fayt, C., Finkenzeller,
 1434 H., Garcia-Nieto, D., Gielen, C., Gómez-Martín, L., Hao, N., Henzing, B., Herman, J. R., Hermans, C.,
 1435 Hoque, S., Irie, H., Jin, J., Johnston, P., Khayyam Butt, J., Khokhar, F., Koenig, T. K., Kuhn, J., Kumar,
 1436 V., Liu, C., Ma, J., Merlaud, A., Mishra, A. K., Müller, M., Navarro-Comas, M., Ostendorf, M., Pazmino,
 1437 A., Peters, E., Pinardi, G., Pinharanda, M., Pitters, A., Platt, U., Posttylyakov, O., Prados-Roman, C.,
 1438 Puentedura, O., Querel, R., Saiz-Lopez, A., Schönhardt, A., Schreier, S. F., Seyler, A., Sinha, V., Spinei,
 1439 E., Strong, K., Tack, F., Tian, X., Tiefengraber, M., Tirpitz, J.-L., van Gent, J., Volkamer, R., Vrekoussis,
 1440 M., Wang, S., Wang, Z., Wenig, M., Wittrock, F., Xie, P. H., Xu, J., Yela, M., Zhang, C., and Zhao,
 1441 X.: Intercomparison of NO₂, O₄, O₃ and HCHO slant column measurements by MAX-DOAS and zenith-
 1442 sky UV–visible spectrometers during CINDI-2. *Atmos. Meas. Tech.*, 13(5), 2169-2208,
 1443 <https://doi.org/10.5194/amt-13-2169-2020>, 2020
 1444
- 1445 Kumar, V., Beirle, S., Dörner, S., Mishra, A. K., Donner, S., Wang, Y., Sinha, V., and Wagner, T. (2020). Long-
 1446 term MAX-DOAS measurements of NO₂, HCHO, and aerosols and evaluation of corresponding satellite
 1447 data products over Mohali in the Indo-Gangetic Plain. *Atmos. Chem. Phys.*, 20(22), 14183-14235.
 1448 doi:10.5194/acp-20-14183-2020
 1449
- 1450
- 1451 Kumar, V., & Sinha, V. (2021), Season-wise analyses of VOCs, hydroxyl radicals and ozone formation chemistry
 1452 over north-west India reveal isoprene and acetaldehyde as the most potent ozone precursors throughout the
 1453 year. *Chemosphere*, 283, 131184. doi:<https://doi.org/10.1016/j.chemosphere.2021.131184>
 1454
 1455

1456 Kurucz, R. L., Furenlid, I., Brault, J., and Testerman, L. : Solar Flux Atlas from 296 to 1300 nm.
 1457 Natl. Sol. Obs., Sunspot, New Mexico, 240, 1984
 1458
 1459 Lee, M., Heikes, B. G., Jacob, D. J., Sachse, G., and Anderson, B. : Hydrogen peroxide, organic hydroperoxide,
 1460 and formaldehyde as primary pollutants from biomass burning, J. Geophys. Res., 102(D1), 1301-1309,
 1461 <https://doi.org/10.1029/96JD01709>, 1997
 1462
 1463
 1464
 1465
 1466
 1467
 1468
 1469
 1470
 1471 Lin, S.-J., & Rood, R. B. : Multidimensional flux-form semi-Lagrangian transport schemes. Mon. Weather Rev.,
 1472 124(9), 2046-2070, [https://doi.org/10.1175/1520-0493\(1996\)124<2046:MFFSLT>2.0.CO;2](https://doi.org/10.1175/1520-0493(1996)124<2046:MFFSLT>2.0.CO;2), 1996
 1473
 1474 Ma, J., Beirle, S., Jin, J., Shaiganfar, R., Yan, P., and Wagner, T. : Tropospheric NO₂ vertical column densities
 1475 over Beijing: results of the first three years of ground-based MAX-DOAS measurements (2008–2011) and
 1476 satellite validation, Atmos. Chem. Phys., 13(3), 1547-1567, <https://doi.org/10.5194/acp-13-1547-2013>,
 1477 2013
 1478
 1479
 1480 Mallik, C., & Lal, S. : Seasonal characteristics of SO₂, NO₂, and CO emissions in and around the Indo-Gangetic
 1481 Plain, Environ Monit Assess, 186(2), 1295-1310, <https://doi.org/10.1007/s10661-013-3458-y>, 2015
 1482
 1483 Martin, R. V., Fiore, A. M., and Van Donkelaar, A. : Space-based diagnosis of surface ozone sensitivity to
 1484 anthropogenic emissions, Geophys. Res. Lett., 31(6), <https://doi.org/10.1029/2004GL019416>, 2004
 1485
 1486

1487 Mahajan, A. S., De Smedt, I., Biswas, M. S., Ghude, S., Fadnavis, S., Roy, C., and van Roozendaal, M. : Inter-
 1488 annual variations in satellite observations of nitrogen dioxide and formaldehyde over India. *Atmos.*
 1489 *Environ.*, 116, 194-201, <https://doi.org/10.1016/j.atmosenv.2015.06.004>, 2015
 1490
 1491
 1492
 1493
 1494
 1495
 1496
 1497 Meller, R., and G. K. Moortgat. : Temperature dependence of the absorption cross sections of formaldehyde
 1498 between 223 and 323 K in the wavelength range 225–375 nm, *J. Geophys. Res.*, 105(D6), 7089-7101,
 1499 doi:10.1029/1999JD901074, 2000
 1500
 1501
 1502
 1503 Mellor, G. L., & Yamada, T. : A hierarchy of turbulence closure models for planetary boundary layers. *J. Atmos.*
 1504 *Sci.*, 31(7), 1791-1806, [https://doi.org/10.1175/1520-0469\(1974\)031<1791:AHOTCM>2.0.CO;2](https://doi.org/10.1175/1520-0469(1974)031<1791:AHOTCM>2.0.CO;2), 1974
 1505
 1506
 1507 Mishra, A. K., and Sinha, V. : Emission drivers and variability of ambient isoprene, formaldehyde and
 1508 acetaldehyde in north-west India during monsoon season, *Environ. Pollut.*, 267, 115538,
 1509 <https://doi.org/10.1016/j.envpol.2020.115538>, 2020
 1510
 1511 Miyazaki, K., Bowman, K., Sekiya, T., Eskes, H., Boersma, F., Worden, H., Livesey, N., Payne, V.H., Sudo, K.,
 1512 Kanaya, Y., Takigawa, M., and Ogochi, K. (2020). Updated tropospheric chemistry reanalysis and
 1513 emission estimates, TCR-2, for 2005–2018. *Earth Syst. Sci. Data*, 12(3), 2223-2259. doi:10.5194/essd-12-
 1514 2223-2020
 1515
 1516

1517 Miyazaki, K., Eskes, H., Sudo, K., Boersma, K. F., Bowman, K., and Kanaya, Y. : Decadal changes in global
 1518 surface NO_x emissions from multi-constituent satellite data assimilation. *Atmos. Chem. Phys.*, 17(2), 807-
 1519 837, <https://doi.org/10.5194/acp-17-807-2017>, 2017
 1520
 1521
 1522 Morino, Y., Ohara, T., Yokouchi, Y., & Ooki, A. : Comprehensive source apportionment of volatile organic
 1523 compounds using observational data, two receptor models, and an emission inventory in Tokyo
 1524 metropolitan area. *J. Geophys. Res.*, 116(D2),doi:<https://doi.org/10.1029/2010JD014762>, 2011
 1525
 1526 Nair, V. S., Moorthy, K. K., Alappattu, D. P., Kunhikrishnan, P.K., George, S., Nair, P. R., Babu, S.S., Abish, A.,
 1527 Satheesh, S.K., Tripathi, S. N., Niranjana, K., Madhavan, B.L., Srikant, V., Dutt, C.B.S., Badarinath,
 1528 K>V>S., & Reddy, R.R.: Wintertime aerosol characteristics over the Indo-Gangetic Plain (IGP): Impacts
 1529 of local boundary layer processes and long-range transport. *J. Geophys. Res.*, 112(D13).
 1530 doi:<https://doi.org/10.1029/2006JD008099>, 2007
 1531
 1532
 1533 Ohara, T., Akimoto, H., Kurokawa, J., Horii, N., Yamaji, K., Yan, X., & Hayasaka, T. : An Asian emission
 1534 inventory of anthropogenic emission sources for the period 1980–2020. *Atmos. Chem. Phys.*, 7(16), 4419-
 1535 4444. doi:<https://doi.org/10.5194/acp-7-4419-2007>, 2007
 1536
 1537
 1538 Platt, U. : Differential optical absorption spectroscopy (DOAS), in *Chemical Analysis Series*, edited, pp. 27-84,
 1539 Wiley & Sons. Inc., 1994
 1540
 1541 Platt, U., and Stutz, J. : *Differential Optical Absorption Spectroscopy*, Springer, 2008
 1542
 1543 Price, C., & Rind, D. : A simple lightning parameterization for calculating global lightning distributions. *J.*
 1544 *Geophys. Res.*, 97(D9), 9919-9933, <https://doi.org/10.1029/92JD00719>, 1992
 1545
 1546
 1547 Rodgers, C. D. : *Inverse methods for atmospheric sounding: theory and practice*, World scientific Singapore, 2008
 1548
 1549 Roscoe, H. K., Van Roozendaal, M., Fayt, C., du Piesanie, A., Abuhassan, N., Adams, C., Akrami, M., Cede, A.,
 1550 Chong, J., Clémer, K., Friess, U., Gil Ojeda, M., Goutail, F., Graves, R., Griesfeller, A., Grossmann, K.,
 1551 Hemerijckx, G., Hendrick, F., Herman, J., Hermans, C., Irie, H., Johnston, P. V., Kanaya, Y., Kreher, K.,

Leigh, R., Merlaud, A., Mount, G. H., Navarro, M., Oetjen, H., Pazmino, A., Perez-Camacho, M., Peters, E., Pinardi, G., Puentedura, O., Richter, A., Schönhardt, A., Shaiganfar, R., Spinei, E., Strong, K., Takashima, H., Vlemmix, T., Vrekoussis, M., Wagner, T., Wittrock, F., Yela, M., Yilmaz, S., Boersma, F., Hains, J., Kroon, M., Piders, A., and Kim, Y. J. : Intercomparison of slant column measurements of NO₂ and O₄ by MAX-DOAS and zenith-sky UV and visible spectrometers. *Atmos. Meas. Tech.*, 3(6), 1629-1646, <https://doi.org/10.5194/amt-3-1629-2010>, 2010

Ryan, R. G., Rhodes, S., Tully, M., & Schofield, R. : Surface ozone exceedances in Melbourne, Australia are shown to be under NO_x control, as demonstrated using formaldehyde: NO₂ and glyoxal: formaldehyde ratios, *Sci. Total Environ.*, 749, 141460, <https://doi.org/10.1016/j.scitotenv.2020.141460>, 2020

Sadavarte, P., & Venkataraman, C. : Trends in multi-pollutant emissions from a technology-linked inventory for India: I. Industry and transport sectors. *Atmos. Environ.*, 99, 353-364. doi:<https://doi.org/10.1016/j.atmosenv.2014.09.081>, 2014

Sarmah, S., Singha, M., Wang, J., Dong, J., Burman, P. K. D., Goswami, S., Ge. Y., Ilyas, S., & Niu, S. : Mismatches between vegetation greening and primary productivity trends in South Asia—A satellite evidence. *Int. J. Appl. Earth Obs.*, 104, 102561. doi:<https://doi.org/10.1016/j.jag.2021.102561>, 2021

Schindlbacher, A., Zechmeister-Boltenstern, S., & Butterbach-Bahl, K. : Effects of soil moisture and temperature on NO, NO₂, and N₂O emissions from European forest soils. *J. Geophys. Res.*, 109(D17), <https://doi.org/10.1029/2004JD004590>, 2004

Schroeder, J. R., Crawford, J. H., Fried, A., Walega, J., Weinheimer, A., Wisthaler, A., Muller, M., Mikovinu, T., Chen, G., Shook, M. : New insights into the column CH₂O/NO₂ ratio as an indicator of near-surface ozone sensitivity. *J. Geophys. Res.*, 122(16), 8885-8907. doi: <https://doi.org/10.1002/2017JD026781>, 2017

Sharma, S., Goel, A., Gupta, D., Kumar, A., Mishra, A., Kundu, S., Chatani, S., and Klimont, Z. : Emission inventory of non-methane volatile organic compounds from anthropogenic sources in India. *Atmos. Environ.*, 102, 209-219. doi:<https://doi.org/10.1016/j.atmosenv.2014.11.070>, 2015

1587 Seco, R., Penuelas, J., and Filella, I. : Short-chain oxygenated VOCs: Emission and uptake by plants and
 1588 atmospheric sources, sinks, and concentrations, *Atmos. Environ.*, 41(12), 2477-2499,
 1589 <https://doi.org/10.1016/j.atmosenv.2006.11.029>, 2007
 1590
 1591
 1592
 1593 Sekiya, T., & Sudo, K. : Roles of transport and chemistry processes in global ozone change on interannual and
 1594 multidecadal time scales. *J. Geophys. Res.*, 119(8), 4903-4921.
 1595 doi:<https://doi.org/10.1002/2013JD020838>, 2014
 1596
 1597 Sekiya, T., Miyazaki, K., Ogochi, K., Sudo, K., & Takigawa, M. : Global high-resolution simulations of
 1598 tropospheric nitrogen dioxide using CHASER V4.0. *Geosci. Model Dev.*, 11(3), 959-988.
 1599 <http://doi.org/10.5194/gmd-11-959-2018>, 2018
 1600
 1601 Seinfeld, J. H., & Pandis, S. N. : Atmospheric chemistry and physics: from air pollution to climate change: John
 1602 Wiley & Sons, New York, 1998
 1603
 1604 Sindelarova, K., Markova, J., Simpson, D., Huszar, P., Karlicky, J., Darras, S., & Granier, C. : High-resolution
 1605 biogenic global emission inventory for the time period 2000–2019 for air quality modelling. *Earth Syst.*
 1606 *Sci. Data*, 14(1), 251-270. doi:<https://doi.org/10.5194/essd-14-251-2022>, 2022
 1607
 1608 Singh, H., Salas, L., Chatfield, R., Czech, E., Fried, A., Walega, J., Evans, M.J., Field, B.D., Jacob, D.J., Blake,
 1609 D., Heikes, B., Talbott, R., Sachse, G., Crawford, J.H., Avery, M.A., Sandholm, S., and Fuelberg, H. :
 1610 Analysis of the atmospheric distribution, sources, and sinks of oxygenated volatile organic chemicals based
 1611 on measurements over the Pacific during TRACE-P, *J. Geophys. Res.*, 109(D15),
 1612 <https://doi.org/10.1029/2003JD003883>, 2004
 1613
 1614 Sinreich, R., Frieß, U., Wagner, T., and Platt, U. : Multi axis differential optical absorption spectroscopy (MAX-
 1615 DOAS) of gas and aerosol distributions, *Faraday discuss.*, 130, 153-164,
 1616 <https://doi.org/10.1039/B419274P>, 2005
 1617
 1618

1619 Solomon, S., Portmann, R., Sanders, R., Daniel, J., Madsen, W., Bartram, B., and Dutton, E. : On the role of
 1620 nitrogen dioxide in the absorption of solar radiation, *J. Geophys. Res.*, 104(D10), 12047-12058,
 1621 <https://doi.org/10.1029/1999JD900035>, 1999
 1622
 1623
 1624 Souri, A. H., Nowlan, C. R., Wolfe, G. M., Lamsal, L. N., Miller, C. E. C., Abad, G. G., Janz, S., Fried, A., Blake,
 1625 D. R., Weinheimer, A. J. , Diskin, G.S., Liu, X., and Chance, K. : Revisiting the effectiveness of
 1626 HCHO/NO₂ ratios for inferring ozone sensitivity to its precursors using high resolution airborne remote
 1627 sensing observations in a high ozone episode during the KORUS-AQ campaign. *Atmos. Environ.*, 224,
 1628 117341, <https://doi.org/10.1016/j.atmosenv.2020.117341>, 2020
 1629
 1630
 1631 Sudo, K., & Akimoto, H. (2007). Global source attribution of tropospheric ozone: Long-range transport from
 1632 various source regions. *J. Geophys. Res.*, 112(D12), <https://doi.org/10.1029/2006JD007992>, 2007
 1633
 1634 Sudo, K., Takahashi, M., Kurokawa, J., & Akimoto, H. : CHASER: A global chemical model of the troposphere
 1635 1. Model description. *J. Geophys. Res.*, 107, 4339, <https://doi.org/10.1029/2001JD001113>, 2002
 1636
 1637 Surl, L., Palmer, P. I., & González Abad, G. : Which processes drive observed variations of HCHO columns over
 1638 India? *Atmos. Chem. Phys.*, 18(7), 4549-4566 ,<https://doi.org/10.5194/acp-18-4549-2018>, 2018
 1639
 1640
 1641 Takemura, T., Nozawa, T., Emori, S., Nakajima, T. Y., & Nakajima, T. : Simulation of climate response to aerosol
 1642 direct and indirect effects with aerosol transport-radiation model. *J. Geophys. Res.*, 110(D2),
 1643 <https://doi.org/10.1029/2004JD005029>, 2005
 1644
 1645 Takemura, T., Egashira, M., Matsuzawa, K., Ichijo, H., O'ishi, R., & Abe-Ouchi, A. : A simulation of the global
 1646 distribution and radiative forcing of soil dust aerosols at the Last Glacial Maximum. *Atmos. Chem. Phys.*,
 1647 9(9), 3061-3073, <https://doi.org/10.5194/acp-9-3061-2009>, 2009
 1648

1649 Tonnesen, G. S., & Dennis, R. L. (2000). Analysis of radical propagation efficiency to assess ozone sensitivity to
 1650 hydrocarbons and NO_x: 1. Local indicators of instantaneous odd oxygen production sensitivity. *J. Geophys.*
 1651 *Res.*, 105(D7), 9213-9225. doi:<https://doi.org/10.1029/1999JD900371>
 1652
 1653
 1654 Vandaele, A., C. Hermans, P. Simon, M. Van Roozendael, J. Guilmot, M. Carleer, and R. Colin.: Fourier
 1655 transform measurement of NO₂ absorption cross-section section in the visible range at room temperature,
 1656 *J. Atmos. Chem.*, 25(3), 289-305, doi:10.1007/BF00053797, 2009
 1657
 1658
 1659 Vandaele, A. C., C. Fayt, F. Hendrick, C. Hermans, F. Humbled, M. V. Roozendael, M. Gil, M. Navarro, O.
 1660 Puertedura, M. Yela, G. Braathen, K. Stebel, K. Tornkvist, P. Jhonston, K. Kreher, F. Goutail, F. Mieville,
 1661 J.P. Pommereau, S. Khaikine, A. Richter, H. Oetjen, F. Wittrock, S. Bugarski, U. Friess, K. Pfeilsticker,
 1662 R. Sinreich, T. Wagner, G. Corlett, and R. Leigh), An intercomparison campaign of ground-based UV-
 1663 visible measurements of NO₂, BrO, and OClO slant columns Methods of analysis and results for NO₂, *J.*
 1664 *Geophys Res*, 110(D8),2005
 1665
 1666
 1667 Vigouroux, C., Hendrick, F., Stavrakou, T., Dils, B., De Smedt, I., Hermans, C., Merlaud, A., Scolas, F., Senten,
 1668 C., Vanhaelewyn, G., Fally, S., Carleer, M., Metzger, J.-M., Müller, J.-F., Van Roozendael, M., and De
 1669 Mazière, M.: Ground-based FTIR and MAX-DOAS observations of formaldehyde at Réunion Island and
 1670 comparisons with satellite and model data, *Atmos. Chem. Phys.*, 9(24), 9523-9544,
 1671 <https://doi.org/10.5194/acp-9-9523-2009>, 2009
 1672
 1673
 1674
 1675
 1676 Wagner, T., Dix, B. v., Friedeburg, C. v., Frieß, U., Sanghavi, S., Sinreich, R., & Platt, U. : MAX-DOAS O₄
 1677 measurements: A new technique to derive information on atmospheric aerosols—Principles and
 1678 information content. *J. Geophys. Res.*, 109(D22). doi: <https://doi.org/10.1029/2004JD004904>, 2004
 1679

1680 Wagner, T., Burrows, J., Deutschmann, T., Dix, B., Friedeburg, C. v., Frieß, U., Iwabuchi, H., Hendrick, F., Heue,
 1681 K.-P., Irie, H., Iwabuchi, H., Kanaya, Y., Keller, J., McLinden, C. A., Oetjen, H., Palazzi, E., Petritoli, A.,
 1682 Platt, U., Postlyakov, O., Pukite, J., Richter, A., van Roozendaal, M., Rozanov, A., Rozanov, V., Sinreich,
 1683 R., Sanghavi, S., and Wittrock, F. : Comparison of box-air-mass-factors and radiances for Multiple-Axis
 1684 Differential Optical Absorption Spectroscopy (MAX-DOAS) geometries calculated from different
 1685 UV/visible radiative transfer models. *Atmos. Chem. Phys.*, 7(7), 1809-1833.
 1686 doi:<https://doi.org/10.5194/acp-7-1809-2007>, 2007
 1687
 1688
 1689 Wang, T., Hendrick, F., Wang, P., Tang, G., Clémer, K., Yu, H., Fayt, C., Hermans, C., Gielen, C., Müller, J.-F.,
 1690 Pinardi, G., Theys, N., Brenot, H., and Van Roozendaal, M. : Evaluation of tropospheric SO₂ retrieved
 1691 from MAX-DOAS measurements in Xianghe, China. *Atmos. Chem. Phys.*, 14(20), 11149-11164,
 1692 <https://doi.org/10.5194/acp-14-11149-2014>, 2014
 1693
 1694
 1695
 1696
 1697 Wesely, M. : Parameterization of surface resistances to gaseous dry deposition in regional-scale numerical models.
 1698 *Atmos. Environ.*, 41, 52-63. <https://doi.org/10.1016/j.atmosenv.2007.10.058>, 1989
 1699
 1700 Williams, J. E., Boersma, K. F., Sager, P. L., & Verstraeten, W. W.,. The high-resolution version of TM5-MP for
 1701 optimized satellite retrievals: description and validation. *Geosci. Model Dev.*, 10(2), 721-750.
 1702 doi:<https://doi.org/10.5194/gmd-10-721-2017>, 2017
 1703
 1704
 1705 Wittrock, F., Oetjen, H., Richter, A., Fietkau, S., Medeke, T., Rozanov, A., and Burrows, J. : MAX-DOAS
 1706 measurements of atmospheric trace gases in Ny-Ålesund-Radiative transfer studies and their application,
 1707 *Atmos. Chem. Phys.*, 4(4), 955-966, <https://doi.org/10.5194/acp-4-955-2004>, 2004
 1708
 1709

1710 Woo, J-H., Kim, Y. , Kim, H-K., Choi, K-C., Eum, J-H., Lee, J-B., Lim, J-H., Kim,J., and Seong, M. : Development
1711 of the CREATE inventory in support of integrated climate and air quality modeling for Asia. Sustainability,
1712 12(19), 7930. doi:<https://doi.org/10.3390/su12197930>, 2020
1713
1714
1715